J. Fluid Mech. (2007), *vol.* 591, *pp.* 183–213.
doi:10.1017/S0022112007008142 Printed in the United Kingdom

Gridless simulations of splashing processes and near-shore bore propagation

M. LANDRINI[1,2,†] A. COLAGROSSI[1‡] M. GRECO[1] AND M. P. TULIN[2]

[1]INSEAN, The Italian Ship Model Basin, Via di Vallerano 139, 00128 Roma, Italy

[2]Ocean Engineering Laboratory, UCSB, California, USA
mpt6@cox.net

(Received 14 October 2005 and in revised form 22 June 2007)

The generation and evolution of two-dimensional bores in water of uniform depth and on sloping beaches are simulated through numerical solution of the Euler equations using the smoothed particle hydrodynamics (SPH) method, wherein particles are followed in Lagrangian fashion, avoiding the need for computational grids. In water of uniform depth, a piston wavemaker produces cyclically breaking bores in the Froude number range 1.37–1.82, which were shown to move at time-averaged speeds in very good agreement with the requirements of global mass and momentum conservation. A single Strouhal number for the breaking period was discovered. Complex repetitive splashing patterns are observed and described, involving forward jet formation growth, impact and ricochet, and similarly, backward jet formation and impact. Observed consequences were the creation of vortical regions of both signs, dipole creation through pairing, large-scale transport of surface water downward and high tangential scouring velocities on the bed, which are quantified. These bores are further allowed to rise on linear slopes to the shoreline, where they are seen to collapse into a tongue-like flow resembling dam-break evolution.

This essentially inviscid calculation is able to reproduce the development of a highly vortical flow in excellent agreement with experimental observations and theoretical concepts. The turbulent flow behaviour is partially described by the numerical solution.

1. Introduction

The reflection of the energy of waves progressing onto the coastal slope is generally weak, long wind waves and swell approaching the shoreline are commonly observed to break offshore and near the shoreline, and thereby dissipate their energy, leading to bottom and shore erosion and to transport of sediment. These breakers can develop as plunging breakers or can occur as quasi-steady spilling breakers or bores (see Peregrine 1983). The practical consequences of near-shore bore phenomena motivated an increasing research effort in this field. Semi-analytical theories of quasi-steady breakers have been developed for bores (Svendsen, Madsen & Hansen 1978) and for deep-water spilling breakers (Cointe & Tulin 1994); useful information has also been obtained from experimental observations, for example by Lin & Hwung (1992). Great

† Deceased 26 June 2003.
‡ Author to whom correspondence should be addressed.

advances have been made in the consideration of water-wave propagation by using boundary-element methods up through the formation of a plunging breaker, both in deep water (Dold & Peregrine 1986; Wang, Yao, & Tulin 1995) and in shallow water and on beaches (Grilli, Svendsen & Subramanya 1997). However, better computer programs, which include the nonlinearity of the Euler equations and can handle the post-breaking evolution, are required.

The numerical simulation of breaking waves has challenged several authors, and here we present our contribution in this direction. We discuss results for bores propagating in water with uniform depth and rising beaches with constant slope.

Breaking bores involve energetic splashing processes and generally a complex fluid dynamics. This is why they are largely discussed only in the experimental literature. In the observed pre-breaking evolution, waves steepen, become asymmetric, and eventually overturn in the form of a forward-plunging jet hitting the free surface. This leads to the formation of a first cavity with large circulation entrapping air (Peregrine 1983). From the plunge point on and within the outer-surf region, creation of coherent and repeatable vortical structures is observed (cf. Svendsen *et al.* 1978). These vortical structures have a topological origin, that is the fluid viscosity is not involved in their formation (Battjes 1988). However, as time goes on, viscosity tends to dissipate the vorticity according to the features involved (i.e. strength and curvature of the vorticity).

The impact of the jet causes the water to splash up cyclically, as observed by Miller (1976), though usually with decreasing strength. The vortical structures (or vortex patches) are made in pairs; one patch rotating clockwise, the other counterclockwise. Usually, the splashing-up water is seen to curl forward, originating a series of co-rotating vortices. In deep-water conditions, Bonmarin (1989) documented that the splash-up also evolved into a backward-facing plunging jet, and then into a counter-rotating vortical structure. Consistent observations in finite water depth have been reported in Jansen (1986) and in Lin & Hwung (1992).

Most of the numerical investigations on breaking waves and subsequent post-breaking evolutions have been performed through field solvers using fixed grids. The free-surface motion is often tracked by marker-and-cell (MAC), volume-of-fluid (VOF) and, more recently, level-set methods. The solutions presented are for two-dimensional problems, with or without the periodicity constraint. A detailed review of such methods for wave hydrodynamics can be found, for instance, in Lin & Liu (1999).

Within the one-fluid (liquid) approaches, the influence of different schemes to discretize the field equations has been examined by Lemos (1996) who studied undular non-breaking bores and the initial evolution of a breaking bore and documented different solutions using different solvers.

Within the two-fluid (liquid and gas) methods, Abadie, Caltagirone & Watremez (1998) applied a VOF technique to analyse the breaking of a large Stokes wave in a periodic domain. The fluid motion associated with the splash-up was tracked by passive Lagrangian markers distributed in a subdomain. For similar initial conditions, Chen *et al.* (1999) studied the breaking using gas and liquid phases with different properties from those of air and water. Surface-tension effects in the pre-breaking regime have been discussed. Finally, consistently with the physical observations by Bonmarin (1989), two different modes were associated with the splash-up.

The turbulent features of the flow in the surf zone have been numerically discussed by Lin & Liu (1998), Bradford (2000) and Christensen & Deigaard (2001). Finite-difference techniques were applied using VOF in the first two works, and MAC

in the last one, to track regular waves approaching a sloping beach. In the first two papers, a k–ϵ model has been adopted with different turbulent closure schemes. Details of the breaking kinematics are not discussed because of the limited numerical resolution, but good agreement with measured mean quantities is reported. Christensen & Deigaard adopted a large eddy simulation (LES) approach assuming the free surface uniform alongshore, but describing the flow underneath as three-dimensional.

The method adopted in the present paper largely differs from the previously mentioned approaches. It is based on a Lagrangian meshless method called smoothed particle hydrodynamics (SPH) particularly suitable for handling free-surface breaking and fragmentation (see e.g. Monaghan 1994, 2005; Monaghan & Kos 2000). Within the SPH algorithm, the fluid is decomposed into a large number of particles, each carrying physical primitive information (density and velocity), and interacting with neighbouring particles according to evolution equations which follow from discretizing the field equations. The particles are moved according to the local fluid velocity, which results in a Lagrangian method featuring an intrinsic tracking of the free surface and self-adaptivity to its large deformations. In the weakly compressible version here implemented, the method is fully explicit and does not require matrix inversions, giving a good computational efficiency and low memory requirements. The method, originally introduced by Gingold & Monaghan (1977) and Lucy (1977) has been greatly enhanced in terms of accuracy and stability properties and widened in applications in the last three decades, mainly by Monaghan and his co-authors (Monaghan 2005). Several theoretical studies have become available for examining on a rigorous basis the properties of the method (Raviart 1985; Mas-Gallic & Raviart 1987; Di Lisio, Grenier & Pulvirenti 1998; Moussa & Vila 2000). In particular, Mas-Gallic & Raviart (1987) have shown that the SPH interpolation (see § 2) is convergent to the second order inside the domain, when the discretization is not introduced. The convergence of present simulations has been checked heuristically as described in Colagrossi & Landrini (2003) and in Le Touzé & Colagrossi (2005). First, SPH applications to free-surface flows have been proposed by Monaghan (1994). More recently, the method has been successfully applied to marine and coastal hydrodynamic problems, such as the breaking of a dam (Colicchio *et al.* 2002), long-time sloshing evolutions in closed water tanks (Landrini, Colagrossi & Faltinsen 2003), and breaking waves on sloping beaches without (Monaghan & Kos 1999) and with a body (Monaghan, Kos & Issa 2003). Applications to finite-(low-) Reynolds-number flows were presented in Takeda, Miyama & Sekiya (1994) and in Morris, Fox & Zhu (1997). Applications to turbulent compressible flows have been shown in Welton & Pope (1997). Bicknell (1991) noticed the formal correspondence between the filtering approach, forming the mathematical basis of the large-eddy simulation, and the smoothing integral (cf. Eq. (2.1)) used to derive the SPH equations, and pointed out the need for additional terms in the SPH equations to model the unresolved scales. Here, the Euler-based SPH model described in Colagrossi & Landrini (2003) has been adopted. Accuracy improvements with respect to the standard SPH method have been achieved through a periodic re-initialization of the density field and the use of a 'ghost particles' technique to model solid boundaries. As in the breaking-bore problem, the fluid viscosity plays a limited role during the generation of the vortical wake, the Euler equation is expected to provide a valuable description of this type of flow. When the viscous effects become relevant, the method may still describe the development of vortical structures and the fragmentation of the free surface during the multiple splash process.

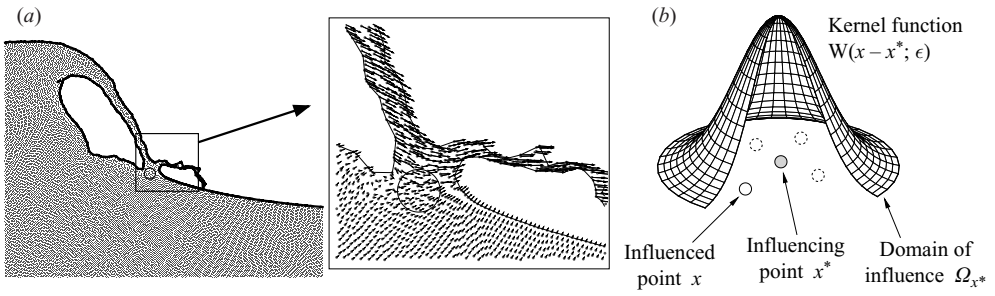

FIGURE 1. (*a*) Typical distribution of particles, ●, in a free-surface flow. In the enlarged detail, the circle represents the radius of interaction of a generic particle. (*b*) Schematic view of the kernel W_ϵ centred on the position $\boldsymbol{x}^\star$.

In the modelling, we will consider only two-dimensional problems whereas the long-time evolution of vortical structures is strongly three-dimensional. A two-dimensional investigation enables us to characterize qualitatively the main features of the breaking and post-breaking evolution and allows us to identify more easily the relevant parameters involved. Further, it leads to a substantial reduction of the CPU-time costs with respect to a three-dimensional simulation. This is crucial when long-time investigations are of interest, as in the present case. However, there are no limits for an extension of the SPH method to treat three-dimensional flows, as demonstrated in Le Touzé & Colagrossi (2005).

Finally, the dynamic action of the entrapped air and the surface tension are not considered. The former approximation is stringent from a quantitative view point; experiments (Lamarre & Melville 1991) have documented the large role of the entrapped air in the dynamics of breaking. The presence of the air will mainly affect the persistence of the vortical structures near the free surface, owing to the involved buoyancy, and introduce a high-frequency oscillating behaviour of the local pressure field. However, the focus of this paper is to identify the main mechanisms involved in the post-breaking evolution and to discuss their influence in terms of links and correlations with the flow features.

Surface tension has a large effect on the foam and white water generated by breaking, but not on the large-scale dynamic processes, so that its neglect is not felt to be serious.

2. Numerical modelling

The main features of SPH method adopted for the present investigation are given in the following; a more detailed description can be found in Colagrossi & Landrini (2003).

Consider a set of N particles distributed over the bulk of fluid Ω, as in the example in figure 1(*a*). Each particle is associated with a *kernel* (or *smoothing*) function W_ϵ (see § 2.1). Each particle moves in the force field generated by the entire particle system and the physical fluid properties evolve according to suitable evolution laws. Conservation of mass is intrinsically assured since each particle has a constant mass all along the simulation. Density variations, however, result from changes in the average spacing among the particles, as reflected by $\mathrm{d}\rho_i/\mathrm{dt}$ in equation (2.5*a*), given later in the text.

The essential features of the resulting algorithm are the complete absence of a computational grid and a fully Lagrangian character (for a discussion of gridless methods see e.g. Belytschko *et al.* 1996; Fries & Matthies 2004).

2.1. *SPH integral interpolation*

In meshless methods, the field of a generic quantity f is represented through convolution integrals over the entire fluid domain Ω. A regularized (smoothed) representation of f at the position $\boldsymbol{x}$ is given by the interpolation integral

$$\langle f(\boldsymbol{x})\rangle = \int_{\Omega} f(\boldsymbol{x}^\star)\, W_\epsilon(\boldsymbol{x}-\boldsymbol{x}^\star)\, \mathrm{d}V^\star, \tag{2.1}$$

over the whole fluid domain Ω. For an efficient solution algorithm, the influence domain $\Omega_{\boldsymbol{x}^\star}$ of the kernel function W_ϵ, must be bounded ($\Omega_{\boldsymbol{x}^\star} \subset \Omega$, as shown in figure 1*b*). In W_ϵ, the parameter ϵ measures the extension of $\Omega_{\boldsymbol{x}^\star}$. W_ϵ is symmetric, regular, non-negative, centred in $\boldsymbol{x}^\star$ and decreases monotonically with $\|\boldsymbol{x}-\boldsymbol{x}^\star\|$ to reach zero at the border of the support $\Omega_{x^\star}$. Its integral on this support is unitary. When $\Omega_{x^\star}$ intersects the boundary $\partial\Omega$ of the fluid domain, the amplitude of the kernel is suitably modified so that its integral is unitary on $\Omega_{x^\star} \cap \Omega$ (see e.g. Belytschko *et al.* 1996). When taking the limit $\epsilon \to 0$, W_ϵ becomes a Dirac delta function and $\langle f\rangle$ coincides exactly with f. The error made in approximating f by its smoothed estimate $\langle f\rangle$ can be determined by expanding the integrand of representation (2.1) as a power series in ϵ. Thus, at the continuous level, the approximation inside the domain results (Mas-Gallic & Raviart 1987),

$$\langle f\rangle = f + O(\epsilon^2). \tag{2.2}$$

However, after the discretization has been introduced, the convergence property does not remain as favourable (see Colagrossi 2005).

The choice of the kernel influences significantly the stability properties of any meshless method (see e.g. Morris 1996). In our computations, three different kernel functions have been investigated: third- and fifth-order splines and a renormalized Gaussian curve. The comparison showed that the last kernel leads to the best stability properties (Morris 1996) and to the largest code efficiency (Colagrossi 2005); moreover, its derivatives can be straightforwardly obtained from the evaluation of the function itself. For these reasons, the renormalized Gaussian kernel has been selected for the present investigation. The corresponding curve is

$$W_\epsilon(\boldsymbol{x}^\star-\boldsymbol{x}) = \frac{\exp(-(s/\epsilon)^2) - \exp(-(\delta/\epsilon)^2)}{2\pi \displaystyle\int_0^\delta s(\exp(-(s/\epsilon)^2) - \exp(-(\delta/\epsilon)^2))\, \mathrm{d}s}, \tag{2.3}$$

where $s = \|\boldsymbol{x}^\star - \boldsymbol{x}\|$. To make its support compact, a cutoff radius δ is introduced, typically set equal to 3ϵ, which corresponds to the same radius as for the classical fifth-order B-spline support (see Monaghan 1992). Obviously, function (2.3) satisfies all the required kernel properties, i.e. symmetry, unit integral over the support, etc.

The SPH formalism (2.1) is mainly used to recover the gradient of a generic field f from its values in the domain. The interpolated gradient of f can be obtained as

$$\begin{aligned}\langle \nabla f\rangle(\boldsymbol{x}) &= \int_{\Omega} \nabla^\star f(\boldsymbol{x}^\star)\, W_\epsilon(\boldsymbol{x}-\boldsymbol{x}^\star)\, \mathrm{d}V^\star \\ &= -\int_{(\Omega\cap\Omega_{x^\star})} f(\boldsymbol{x}^\star)\, \nabla^\star W_\epsilon(\boldsymbol{x}-\boldsymbol{x}^\star)\, \mathrm{d}V^\star \\ &\quad + \int_{\partial(\Omega\cap\Omega_{x^\star})} f(\boldsymbol{x}^\star)\, W_\epsilon(\boldsymbol{x}-\boldsymbol{x}^\star)\, \boldsymbol{n}_{S^\star}\, \mathrm{d}S^\star,\end{aligned} \tag{2.4}$$

in which an integration by parts has been used. In expression (2.4), $\boldsymbol{n}_{S^\star}$ is a unitary vector normal to $\partial(\Omega \cap \Omega_{x^\star})$ and pointing outside $\Omega \cap \Omega_{x^\star}$; further, the surface terms are null when $\partial\Omega_{x^\star}$ is inside the domain Ω, being $W_\epsilon(\boldsymbol{x} - \boldsymbol{x}^\star)$ zero on $\partial\Omega_{x^\star}$. However, when $\Omega_{x^\star} \cap \partial\Omega \neq 0$ the surface term is not null and can be used to enforce the proper boundary conditions of the problem.

2.2. *SPH enforcement of the free-surface and solid boundary conditions*

The free-surface boundary conditions can be handled easily by the SPH method. Owing to the Lagrangian character of the solver, the kinematic condition is intrinsically satisfied while the dynamic condition must be enforced. Within the SPH solution algorithm, the pressure is explicitly required only for the evaluation of ∇p through the interpolation formula (2.4), so the value of the external pressure p_e acting along the free surface can be enforced through the corresponding surface integral term. Here p_e is set to zero, leading to a null free-surface integral term. In general, the modelling of solid boundaries represents a challenge for the SPH methods. The classical techniques use either repellent forces acting along the boundary, or materialize the wall as fixed particles with adequate physical properties (see e.g. Monaghan 2005). Here a 'ghost particles' technique has been employed, which consists in locally mirroring with respect to the solid boundary the fluid layer (and related physical properties) at a distance of less than 3ϵ from the wall. The mirroring leads to an exact free-slip condition on the boundary (see Colagrossi & Landrini 2003) and implies an extension of the calculation domain outside the physical fluid domain Ω. The latter means that also the solid-boundary integral term in expression (2.4) is avoided. The ghost particles approach is more efficient (Monaghan 2005) and handles more accurately the pressure along the wall (Colagrossi & Landrini 2003). This technique has been implemented to model correctly piece-wise straight boundaries. Its extension to more general body shapes is at present under investigation.

2.3. *Basic SPH equations*

Upon inserting the discrete form of formula (2.4) into the Euler equations, after some manipulation (see e.g. Colagrossi & Landrini 2003), the following evolution equations for the density ρ_i, the velocity $\boldsymbol{v}_i$ and the position $\boldsymbol{x}_i$ of the ith particle are obtained:

$$\frac{\mathrm{d}\rho_i}{\mathrm{d}t} = -\rho_i \sum_{j=1}^{N} (\boldsymbol{v}_j - \boldsymbol{v}_i) \cdot \nabla_i W_\epsilon(\boldsymbol{x}_i - \boldsymbol{x}_j)\, \mathrm{d}V_j, \tag{2.5a}$$

$$\frac{\mathrm{d}\boldsymbol{v}_i}{\mathrm{d}t} = -\frac{1}{\rho_i} \sum_{j=1}^{N} (p_i + p_j) \nabla_i W_\epsilon(\boldsymbol{x}_i - \boldsymbol{x}_j)\, \mathrm{d}V_j + \boldsymbol{g}, \tag{2.5b}$$

$$\frac{\mathrm{d}\boldsymbol{x}_i}{\mathrm{d}t} = \boldsymbol{v}_i. \tag{2.5c}$$

Here the subscripts indicate the fluid particles involved and $\mathrm{d}m_j$ is the constant mass carried by the jth particle so that the particle volume results, $\mathrm{d}V_j = \mathrm{d}m_j/\rho_j$. We note that the structure of the discretized momentum equation is symmetric and ensures linear- and angular-momentum conservation (Bonet & Lok 1999).

The fluid is modelled as a (weakly) compressible fluid with a state equation of the form

$$p = \frac{\rho_0 c_0^2}{\gamma} \left[\left(\frac{\rho}{\rho_0} \right)^\gamma - 1 \right], \tag{2.6}$$

with $\gamma = 7$ and c_0 the speed of sound for $\rho = \rho_0$. To remain in the weak compressible regime, the speed of sound $c = \sqrt{\mathrm{d}p/\mathrm{d}\rho}$ must be at least one order of magnitude greater than the maximum flow velocity, in the whole domain Ω and during the entire simulation (Monaghan 1992; Molteni, Colagrossi & Colicchio 2007). For the problems presented in this paper, a good estimation of the maximum flow velocity is twice the velocity of the bore front (therefore c_0 was set equal to twenty times the velocity of the bore front). In practical computations, this choice ensures that the density fluctuations will remain lower than $10^{-2}\rho_0$.

The use of an explicit formula for the pressure avoids the need to solve the Poisson equation, and therefore increases the efficiency and reduces the memory requirements of the method. To obtain a more regular pressure distribution, Colagrossi & Landrini (2003) proposed a periodical 're-initialization' of the density field, based on a moving-least-squares interpolation (see e.g. Belytschko *et al.* 1998), that is, periodically ρ_j is evaluated directly from the mass distribution of the fluid particles using the SPH interpolation strategy. This filters out unphysical high-frequency pressure oscillations.

The implementation of equations (2.5) leads to an unstable solution. To overcome this problem, equations (2.5*b*) and (2.5*c*) have been modified. In particular, the fluid momentum equation has been changed in

$$\frac{\mathrm{d}\boldsymbol{v}_i}{\mathrm{d}t} = -\frac{1}{\rho_i}\sum_{j=1}^{N}(p_i + p_j + \Pi_{ij})\nabla_i W_\epsilon(\boldsymbol{x}_i - \boldsymbol{x}_j)\,\mathrm{d}V_j + \boldsymbol{g} \tag{2.7}$$

Π_{ij} being an artificial stress term between the ith and the jth particles chosen here in the form

$$\Pi_{ij} = -\alpha\epsilon\rho_j\rho_i\frac{c_i + c_j}{\rho_i + \rho_j}\frac{\min[(\boldsymbol{u}_i - \boldsymbol{u}_j)\cdot(\boldsymbol{x}_i - \boldsymbol{x}_j)\,;0]}{|\boldsymbol{x}_i - \boldsymbol{x}_j|^2 + 0.01\epsilon^2}, \tag{2.8}$$

as suggested by Monaghan (1985). The parameter α must be suitably chosen for a stable and accurate solution. In our simulations, its influence has been checked in the range $\alpha \in [0.005\text{–}0.06]$. The use of Π_{ij} corresponds to an equivalent kinematic viscosity of the form $15/112\,\alpha c\epsilon$ (Monaghan 2005). Because ϵ reduces refining the discretization, Π_{ij} also decreases with it.

The equation governing the motion of the particles has been modified as follows:

$$\frac{\mathrm{d}\boldsymbol{x}_i}{\mathrm{d}t} = \boldsymbol{v}_i + 0.5\sum_{j=1}^{N}\frac{\boldsymbol{v}_j - \boldsymbol{v}_i}{(\rho_i + \rho_j)}W_\epsilon(\boldsymbol{x}_i - \boldsymbol{x}_j)\,\mathrm{d}m_j, \tag{2.9}$$

with the additional term aimed to weakly average the velocity field around the considered particle. This correction reduces the particle disorder and weakens the oscillations of the velocity field caused by the weak compressibility of the liquid (see e.g. Monaghan 2005). The evolution equations so obtained can be stepped forward in time by any ODE integrator. In the present implementation, a second-order predictor–corrector scheme was adopted with a dynamic choice of the time step δt according to stability constraints related to (i) the local speed of sound and (ii) the local value of the particle acceleration. The related stability requirements are stringent (a negative aspect of the weakly compressible SPH formulation) and can easily lead locally to a very small time step. To alleviate the problem, an individual time-stepping algorithm (Hernquist & Katz 1989) has been adopted, which allows the particles to evolve hierarchically according to their own time step.

Although the particle evolution equations are coupled, their right-hand sides can be evaluated independently and without the solution of an algebraic system (required

in most of the discretization methods for PDEs). Therefore, the required memory is just proportional to the number N of particles, and the algorithm is well suited for use on parallel computers.

In the SPH method, the characteristic discretization parameters are: (i) the ratio $\epsilon/\mathscr{L}$, where $\mathscr{L}$ is a typical length scale of the problem, and (ii) the parameter ϵ which is related to the number of particles $\mathscr{N}$ within the interaction radius 3ϵ (i.e. the circle in figure 1). Roughly speaking, in two-dimensional problems, the parameter $3\epsilon\sqrt{\pi/\mathscr{N}}$ is the equivalent of the grid size Δx in mesh-based methods. For the problems studied in the following, we considered the mean water depth h_0 as the reference length scale. Further, $\mathscr{N} \simeq 50$ and particle location on a Cartesian uniform lattice (i.e. $\epsilon/\Delta x \simeq 1.33$) were used for the initial configuration in all the simulations. Where not explicitly stated in the paper, an initial spatial resolution $\Delta x = h_0/50$ was adopted (i.e. $\epsilon/h_0 \simeq 0.027$), while the total number of particles depends on the considered case, i.e. on the total length of the domain. In most of the present simulations, a domain length of $60\,h_0$ was assumed, corresponding to about 150 000 particles. All the computations presented have been performed on Pentium III 700 MHz processors. With this CPU, the SPH algorithm used requires a time cost of 50 μs for each particle and each time iteration. The simulations presented here required 24–48 h CPU-time using a memory space smaller than 50 MBytes (double-precision variables have been used).

Since a kernel with a compact support has been adopted (see expression (2.3)), an efficient code can be obtained with an *ad hoc* neighbour search strategy. The latter is important for reducing the CPU time costs of an SPH solver since distances between neighbour particles must be calculated for each time step. Here a *linked-lists* algorithm has been implemented (see e.g. Allen & Tildesley 1987), which at present requires a number of operations only proportional to N.

The numerical method described above has been applied to a large variety of violent free-surface flows and compared with solutions by other solvers, dam-break flows: Colicchio *et al.* (2002), Colagrossi & Landrini (2003); sloshing flows: Landrini *et al.* (2003); jet entry flows: Trivellato, Bertolazzi & Colagrossi (2004); ship flows: Tulin & Landrini (2000), Landrini, Colagrossi & Tulin (2001); wave breaking process: Colagrossi, Landrini & Tulin (2000).

3. Breaking bores

We first study the genesis and propagation of breaking bores over water with uniform depth. The model problem selected is sketched in figure 2: the flow starts with a semi-infinite layer of fluid, depth h_0, forced into motion by a vertical piston, moving from left to right with constant speed U. The actual numerical simulations have been performed with $h_0 = 0.1\,\mathrm{m}$ and $g = 9.81\,\mathrm{m\,s^{-2}}$. In the discussion and in the figures, non-dimensional quantities are used by taking h_0 and $\sqrt{h_0/g}$ as length and time scales, respectively. With these scales, the piston speed U and the celerity of the bore front u are made non-dimensional, respectively, as $F_P = U/\sqrt{gh_0}$ and $F_0 = u/\sqrt{gh_0}$.

At the beginning of the simulation, a smooth ramp-function for the piston velocity has been used to prevent formation of a jet at the solid boundary, which is irrelevant for our purposes.

As time passes, for small velocity of the piston, a non-breaking undular bore develops, reconciling the initial unperturbed water level h_0 with the higher one h_1 behind it. This case can be accurately described by boundary integral equation methods. In Greenhow & Lin (1985), $F_P \sim 0.35$ is given as threshold for the leading

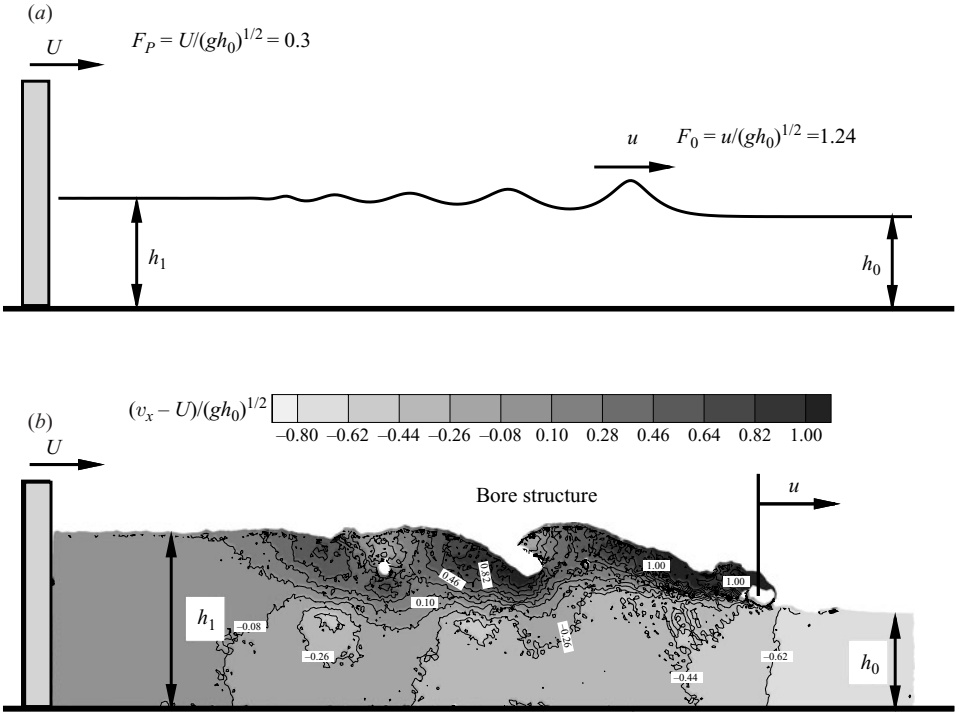

FIGURE 2. Sketches of the bore generated by a piston moving horizontally with velocity U in a layer of fluid with initial depth h_0. (*a*) Generation of a non-breaking undular bore, $F_P = 0.3$. (*b*) Generation of a fully developed breaking bore, $F_P = 0.8$. Contour levels are representative of the fluid horizontal velocity v_x.

F_P	h_1/h_0	F_0	u_{SPH}/u_{th}
0.95	2.12	1.82	1.06
0.90	2.1	1.80	1.00
0.80	1.9	1.66	0.94
0.70	1.8	1.59	1.00
0.60	1.7	1.52	0.98
0.50	1.5	1.37	1.02

TABLE 1. Comparison between the computed velocity, u_{SPH}, of the bore front and the theoretical value, u_{th}, predicted by using global mass and momentum conservations, cf. analytical solution (3.2) for different piston speeds. Main parameters are defined in figure 2.

crest of the undular bore to break (cf. figure 5.4 in Greenhow & Lin 1985). Increasing the velocity of the piston, the undulations disappear and only fully developed breaking bores are observed. This result is consistent with the experiments by Miller (1968), who fixed the transition between undular non-breaking bores and fully developed bores in the range $1.35 \leqslant F_0 \leqslant 1.55$, with u the bore front velocity (cf. analytical solution (3.2) and table 1).

In the following, we are interested in describing surface breaking and we consider the range $0.5 \leqslant F_P \leqslant 0.95$, for which the wavefront steepens rapidly, overturns, and evolves into a breaking bore. Actually, the transition from undular-breaking bores

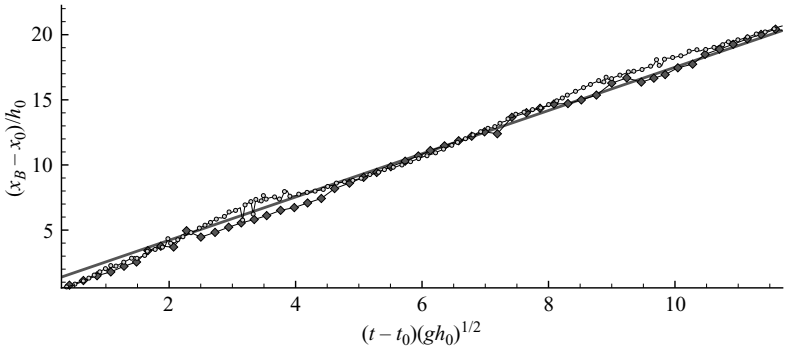

FIGURE 3. Breaking bore for piston-based Froude number $F_P = 0.8$: time history of the average bore-front position x_B. The SPH predictions using two different values of the parameter β (◆, $\beta = 0.22$; ○, $\beta = 0.55$) are compared with the theoretical evolution (—) of the bore-front obtained by integrating expression (3.2). x_0 corresponds to x_B at the initial time t_0. Main parameters are defined in figure 2.

to fully developed breaking bores is gradual (Teles da Silva & Peregrine 1990; Landrini & Tyvand 2001) and, in our simulations, for $F_P = 0.5$ we still observe a train of smooth long undulations downstream of the breaking front.

For the fully developed bores and for a given piston-based Froude number F_P, by using mass and momentum conservation, we can evaluate the ratio between the two mean water levels h_1 and h_0 as

$$\left(\frac{h_1}{h_0} - 1\right)\sqrt{\frac{(1 + h_1/h_0)}{2h_1/h_0}} = F_P \tag{3.1}$$

(see i.e. Stoker 1957). Then the dimensionless velocity of the bore can be related to the water depths,

$$F_0^2 = \left(\frac{u_{\text{th}}}{\sqrt{gh_0}}\right)^2 = \frac{1}{2}\left(\frac{h_1}{h_0}\right)\left(1 + \frac{h_1}{h_0}\right). \tag{3.2}$$

During all the simulations the front of the bore is not sharply defined and this has been also observed in laboratory experiments. After an initial transient the averaged velocity of the front, estimated as the ratio between the average instantaneous bore position, x_B, and the time interval used in the simulation, becomes constant. The related numerical x_B time evolution is presented in figure 3 for the case with $F_P = 0.8$. Here, x_B has been defined as the vertical section where the water depth is equal to $h_0 + \beta(h_1 - h_0)$, with $\beta \in (0.2, 0.8)$. The results show a limited influence of β and compare well with the theoretical x_B evolution obtained by integrating expression (3.2).

The data from our gridless simulations and the theoretical predictions from formula (3.2) are given in table 1.

The agreement is fair within an error within a few per cent. It is perhaps surprising that such good agreement is found with an Euler computation for a flow which is considered highly dissipative. However, we must note that the numerical solution involves both main mechanisms for energy dissipation: (i) molecular viscosity and (ii) conversion to small-scale random eddy like motion. In fact, the artificial stress used numerically behaves as a viscous stress. Further, during the simulation some of the energy in the horizontal motion is lost through the conversion process.

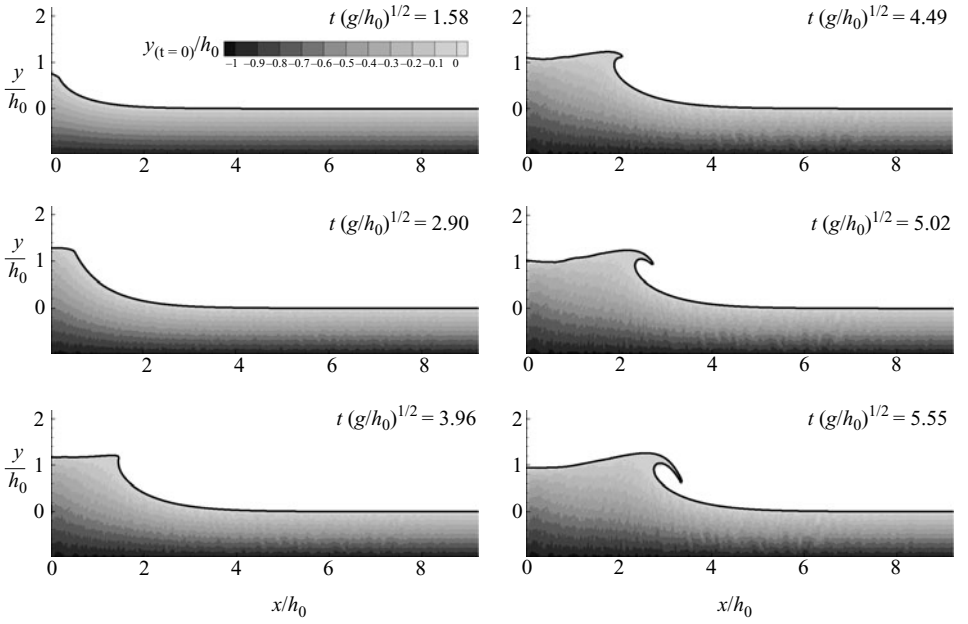

FIGURE 4. Initial evolution of the free-surface motion induced by a vertical piston in steady forward motion, piston-based Froude number $F_P = 0.8$. The coordinate system moves with the piston. The free-surface profiles obtained by a BEM solver (solid lines) are superimposed onto the SPH solution. Contour levels are representative of the vertical heights $y_{(t=0)}$ at initial time $t = 0$ s of the particles simulated by the SPH.

The model problem under analysis is the same as in the experiments described in Miller (1968). Miller (see figure 4 in his paper) observed a larger dispersion of the measured bore velocity u_{front} around the theoretical prediction, with the scattering of measured data increasing rapidly for bores with $h_1/h_0 > 2$. He ascribed this difficulty to the turbulence and aeration of the front, preventing the accurate determination of the bore velocities.

3.1. *Pre-breaking stage*

A typical initial evolution is shown in figure 4 for $F_P = 0.8$. The particles used in the simulation are plotted together with the free-surface profiles obtained by a boundary-element method (BEM), and are marked according to their initial distance from the bottom.

After the piling up of the water against the piston, a long wave starts to propagate with velocity of the order of $\sqrt{gh_0}$ and soon steepens, overturns and breaks with a large plunging jet impacting onto the underlying free surface. The breaking of the free surface prevents the BEM from further following the evolution of the flow field.

The comparison between the two solution methods is satisfactory for all the configurations reported; an enlarged view of the jet region highlights some local differences, as shown in figure 5 for the most critical configuration. The SPH free surface is characterized by a more irregular behaviour. This is because the motion of the fluid particles is followed without any specific smoothing technique whereas in the BEM solver regridding is used during the simulation. A finer SPH description of

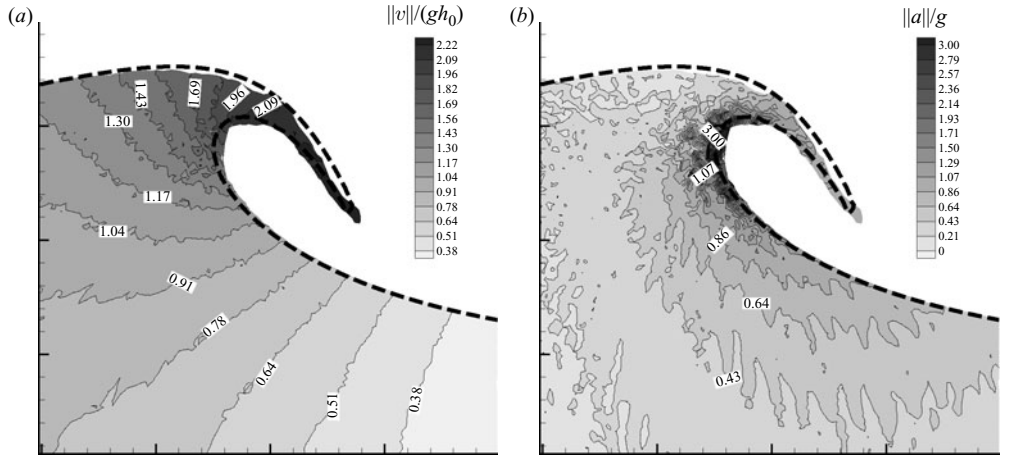

FIGURE 5. Enlarged view of the plunging jet at the last time instant shown in figure 4. The BEM free-surface profile (dashed line) is superimposed onto the SPH solution given in terms of the contours of the (*a*) velocity and (*b*) acceleration fields. Main parameters are defined in figure 2.

small scales within the jet can be obtained by varying ϵ spatially, as discussed in the following sections.

3.2. *Impact and ricochet of the plunging jet*

The forced breaking bore features repeated plunging events. This occurs in shallow water as well as in deep water. A detailed description of the first plunging event in the deep-water case is given in figure 6 for $F_P = 0.8$.

In particular, we have chosen the reference configuration in the top-left-plot and assumed that the jet is formed by the particles, marked by black dots, within the area delimited by the free surface and the vertical line tangent to the nascent loop beneath the jet (see enlarged view). In the following plots, the motion of these particles is tracked by means of the Lagrangian character of the SPH. During the free-falling phase, the jet is stretched and narrows because of mass conservation. At the impact, the jet-particles flow into two separated streams (figure 6*c*). One is deflected inside the loop, and the other one contributes to the formation of the splash-up. Initially, the plunger is fed only by fresh particles which undergo the same evolution as the black particles. Later on, the particles earlier entrapped by the clockwise structure, complete one revolution and (partly) re-contribute to the impinging jet (figure 6*d*, *e*), implying a strong mechanical mixing. The particles entering the splash-up evolve into a new plunger and are again split into a portion captured by a second clockwise structure and a remaining one forming another splash-up (see figure 6*c*).

A portion of the particles originally in the first plunger ride on the moving front of the propagating wave, while the others are captured by the cavities and effectively mixed with other portions of fluid. In the following cycles, all the tracked particles are captured by the rotating structures and fresher particles feed the bore front.

A more quantitative analysis is presented in the two bottom plots in terms of the velocity components of the centre of mass of the jet particles

$$(V_{c,x}, V_{c,y}) = \int_{jet} \rho(v_x, v_y)\,\mathrm{d}A \;\Big/ \int_{jet} \rho\,\mathrm{d}A. \tag{3.3}$$

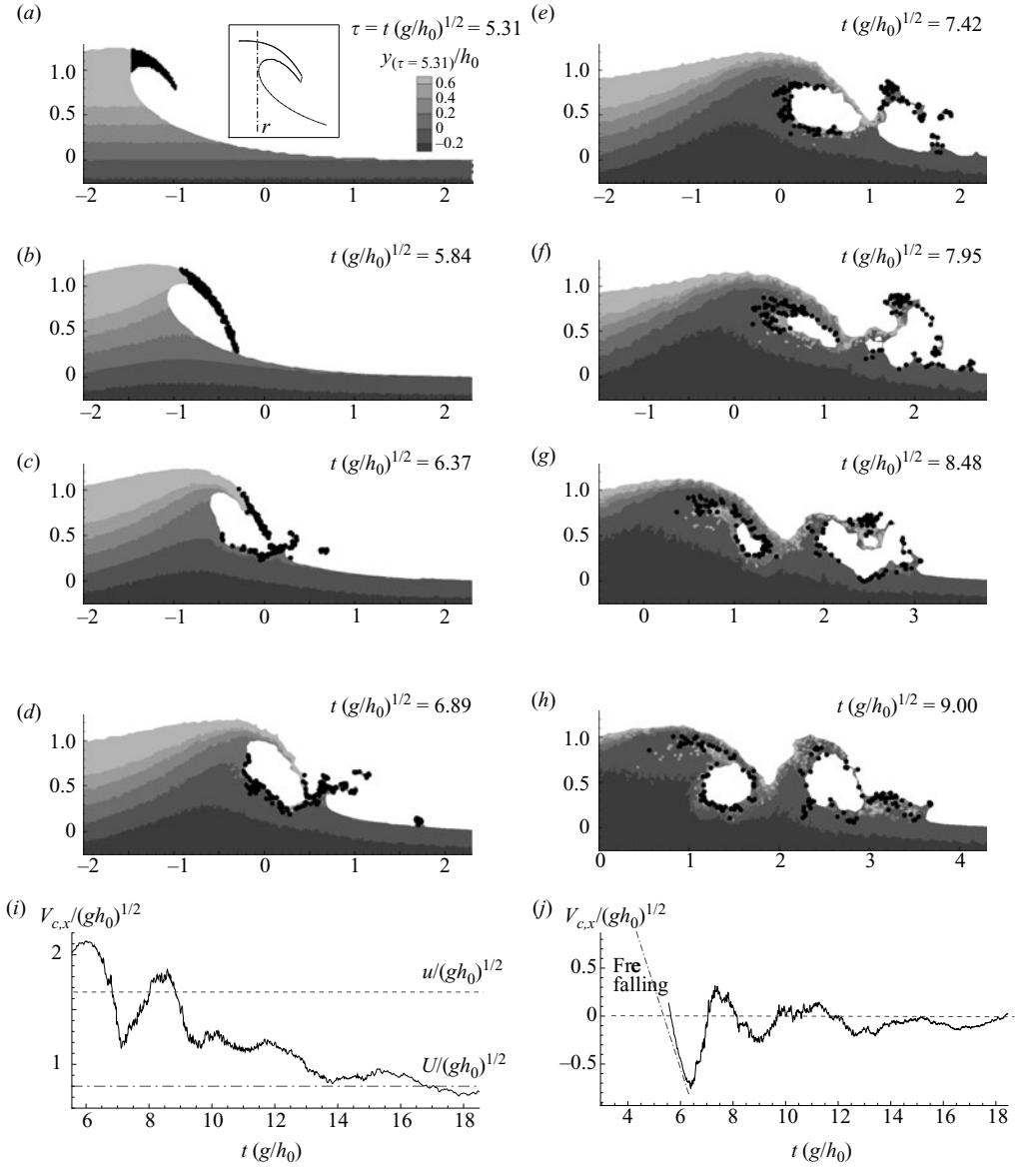

FIGURE 6. Breaking bore for piston based Froude number $F_P = 0.8$: evolution of the particles forming the initial jet (marked by black symbols). Time increases from (*a*) to (*h*). Contour levels are representative of the vertical heights $y_{(\tau=5.31)}$ at the non-dimensional time $\tau = 5.31$ of the particles simulated by the SPH. The two bottom diagrams show the time evolution of the (*i*) horizontal and (*j*) vertical components of the centre of mass of the plunging-jet particles. The dot-dashed and the dashed horizontal lines in (*i*) indicate the piston and bore-front horizontal velocities, respectively. The dot-dashed line in (*j*) represents the vertical-velocity free-fall law. Main parameters are defined in figure 2.

From the results, the first part of the jet evolution is characterized by a free-fall stage accompanied by an almost steady translation in the horizontal direction. The instant of the impact is evidenced by sharp changes of the velocity components. $V_{c,x}$ drops down to half of its initial value when the jet splits into two portions

with backward and forward motion. After some decreasing oscillations, due to both the orbital motion and the multiple splash-up, $V_{c,x}$ attains the uniform velocity of the moving piston. $V_{c,y}$ bounces up, changing in sign, because both fluid portions are moving upwards, and then oscillates consistently with the orbital motion of the particles entrapped in the cavities. Eventually, $V_{c,y}$ attains an almost zero value, with small-amplitude oscillations related to the orbital motion inside the vortical structures rotating in an uncorrelated way.

For problems involving multiple breaking, an important numerical issue is the ability to reproduce accurately the penetration of the plunging jets. In this context, experimental data on the flow field at the plunge point can be useful for a fuller validation of the numerical simulations, as well as for a deeper understanding of the fluid dynamics involved. Comparisons with the potential mixed finite-element model by Trivellato *et al.* (2004) in the case of entry problems with jets of various shapes and intensities proved that the SPH artificial viscous stress Π_{ij} plays a negligible role in the jet penetration dynamics. Surface tension, rounding the developing jet, could play a role and should be examined in future.

The estimation of fluid invariants (mass, momentum, energy, etc.) can be used as a measure of the global accuracy of the method. Mass and momentum (both linear and angular) are conserved by the SPH solver. The energy dissipated during a numerical simulation is investigated in the following for the case with a piston Froude number equal to $F_P = 0.8$.

Generally speaking, the total energy E_t of the fluid is characterized by the mechanical energy E_m (sum of kinetic, E_k, and potential, E_p, terms) and by the internal energy E_u. For the breaking bore problem analysed here, the total energy E_t of the fluid must be equal to the work done by the moving piston on the fluid W_p, i.e.

$$E_t = E_m + E_u \equiv W_p. \tag{3.4}$$

The time evolution equations of the energy terms E_m and E_u, for an inviscid compressible flow, are given by:

$$\rho \frac{\mathrm{d}E_m}{\mathrm{d}t} = -\boldsymbol{v} \cdot \nabla p + \boldsymbol{g} \cdot \boldsymbol{v}, \quad \rho \frac{\mathrm{d}E_u}{\mathrm{d}t} = -p \,\mathrm{div}(\boldsymbol{v}). \tag{3.5}$$

which become:

$$\left[\rho \frac{\mathrm{d}E_m}{\mathrm{d}t}\right]_i = -\boldsymbol{v}_i \cdot \sum_j (p_i + p_j + \Pi_{ij}) \nabla_i W_\epsilon(\boldsymbol{x}_i - \boldsymbol{x}_j)\, \mathrm{d}V_j + \boldsymbol{g} \cdot \boldsymbol{v}_i \tag{3.6a}$$

$$\left[\rho \frac{\mathrm{d}E_u}{\mathrm{d}t}\right]_i = -\sum_j \left(p_i + \frac{1}{2}\Pi_{ij}\right) (\boldsymbol{v}_j - \boldsymbol{v}_i) \cdot \nabla_i W_\epsilon(\boldsymbol{x}_i - \boldsymbol{x}_j)\, \mathrm{d}V_j \tag{3.6b}$$

for the generic ith particle. Here the artificial viscous stress Π_{ij} (see definition (2.8)) is taken into account. Following a procedure similar to that by Benz (1990) it is possible to demonstrate that the discrete equations (3.6) lead to conserving exactly the total energy. Therefore they allow us to evaluate the work W_p through the link (3.4).

A crucial aspect is to investigate the time evolution of the energy loss $E_m - W_p = -E_u$. Sources of E_u are related both to the artificial viscous stress Π_{ij} and to the weakly compressibility assumption. Concerning the latter, in the SPH, the speed of sound adopted is smaller than in reality, and so the numerical divergence of the velocity field can be much larger. For these reasons, E_u does not coincide with the physical internal energy, but can be used to evaluate the numerical dissipation for a given spatial resolution.

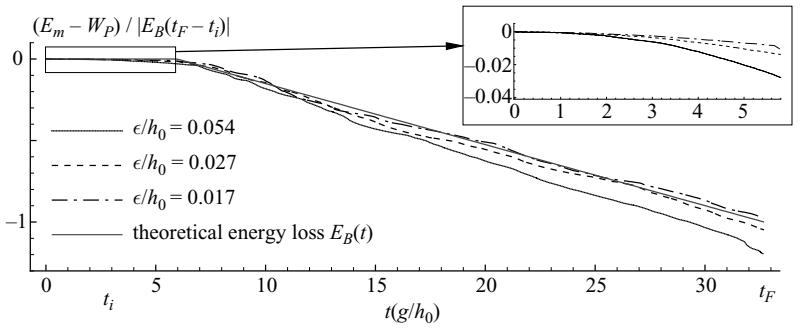

FIGURE 7. Breaking bore for piston-based Froude number $F_P = 0.8$: time evolution of the SPH energy loss $E_m - W_p$, where E_m is the mechanical energy of the fluid and W_p is the work done by the moving piston. $E_m - W_p$ is made non-dimensional by the equivalent energy loss, E_B, evaluated between times t_i and t_f for a theoretical bore modelled as a shock between the two water levels. The numerical results have been obtained with three different spatial resolutions: $\epsilon/h_0 = 0.054, 0.027, 0.017$. Main parameters are defined in figure 2.

In figure 7, the SPH $(E_m - W_p)$ has been compared with the theoretical energy loss

$$E_B(t_f) = -\rho\, g\, h_0\, u\, \frac{(h_1 - h_0)^3}{4\, h_1\, h_0}(t_f - t_i), \tag{3.7}$$

between times t_i and t_f when the bore front is considered as a discontinuity moving with velocity u between the water levels h_0 and h_1 (see e.g. Stoker 1957). Here, $t_i \simeq 6\sqrt{h_0/g}$ is the time when the first plunger impacts the underlying water and $t_f \simeq 33\sqrt{h_0/g}$ is the final time of the simulation. The results show convergence to the theoretical energy loss which is zero in the pre-breaking stage $[0 \ldots t_i)$ and given by formula (3.7) in the post-breaking stage. During the pre-breaking phase, the energy loss is dominated mainly by the artificial viscous stress Π_{ij} and the internal energy E_u converges to zero linearly with the smoothing length ϵ (see e.g. Colagrossi 2005). During the post-breaking stage, the time decay of the energy loss is governed by the transfer of energy to small scale random eddy like motion.

3.3. *Splash-up cycles and formation of vortical structures*

The post-breaking evolution for $F_P = 0.8$ is described in figure 8 starting from the breaking of the plunging jet (figure 8*a*). The impact causes the closure of a cavity and leads to a clockwise-rotating structure (figure 8*b*). A splash-up (I) is formed partially fed by the impinging jet, growing in the form of a mushroom-like upwelling structure (figure 8*c*). A second plunging event is caused, giving rise to a second splash-up (II) and to another clockwise rotating structure, (figure 8*d*).

The formation of the mushroom-like structure and the growth of the backward jet are essentially related to the gravitational collapse of the mass of water which, deflected upwards by the impact, eventually falls down. The further evolution of the backward-facing jet, impacting with the free surface, results in a counterclockwise vortex with a strength similar to that of the first clockwise structure. This fact and their closeness cause the two structures to behave like a dipole. Further, they are sufficiently far from other vortical structures and strong enough to evolve as an isolated dipole in an infinite fluid, i.e. they fall down toward the sea floor (figure 8*e*). Eventually, they are affected by the bottom presence and separate (figure 8*f*, *g*). Two main aspects are necessary for such evolution: (*a*) the strength of the backward jet, responsible for the counterclockwise vortex, must be similar to the strength of the

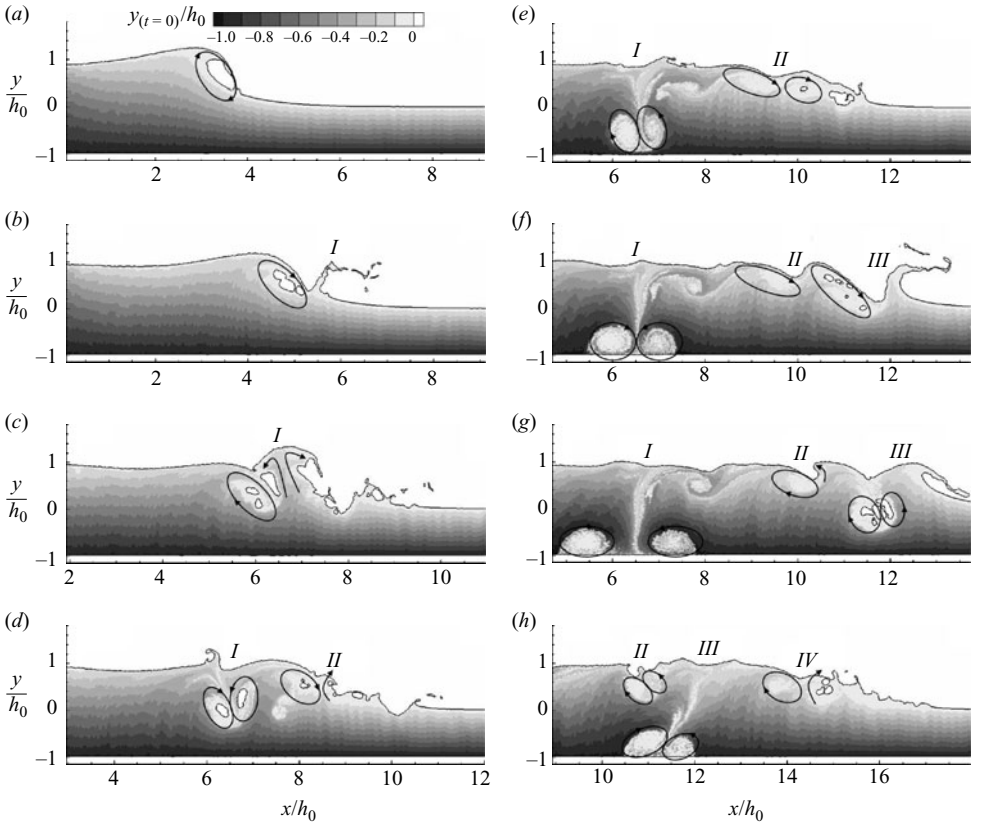

FIGURE 8. Breaking bore for piston-based Froude number $F_P = 0.8$: further evolution of the case presented in figure 4 as predicted by the SPH solver. (*a*) to (*h*) correspond to non-dimensional time instants $t(g/h_0)^{1/2} = 5.94$, 7.92, 10.2, 11.4, 13.2, 14.6, 16.0 and 18.7, respectively. The main features observed are as follows. (*a*) Initial impact of the plunging jet. (*b*) Closure of a cavity and related clockwise rotating structure. (*c*) Mushroom-like upwelling structure. (*d*) Second plunging event and related clockwise rotating structure. (*e*) Dipole-like structure at the sea bed. (*f*–*h*) Breaking of the first and third dipole-like structures owing to the interaction with the bottom. Contour levels are representative of the vertical heights $y_{(t=0)}$ at initial time $t = 0$ s. of the particles simulated by the SPH. Main parameters are defined in figure 2.

earlier forward jet, causing the clockwise vortex, and (*b*) the two (backward and forward) jets must be relatively energetic.

The weakness of the forward jet connected with the splash-up II delays the formation of a subsequent backward flow and of the related counterclockwise structure. The latter pairs with the earlier clockwise vortex leading to a dipole-like structure that falls down (figure 8*h*). Later, a third splash-up (*III*) originates with similar strength to the splash-up *I*. The subsequent dipole-like structure is quite strong and falls down earlier than the corresponding structure created by the splash-up *II*.

The described interaction phenomena resemble modes A and B observed experimentally by Bonmarin (1989) for breaking surface waves in deep water. Mode A is connected with the weak impact of water against the underlying free surface resulting in shearing layers above the vortical structures. Mode B is associated with more intense impacts leading to the formation of pronounced backward-facing jets.

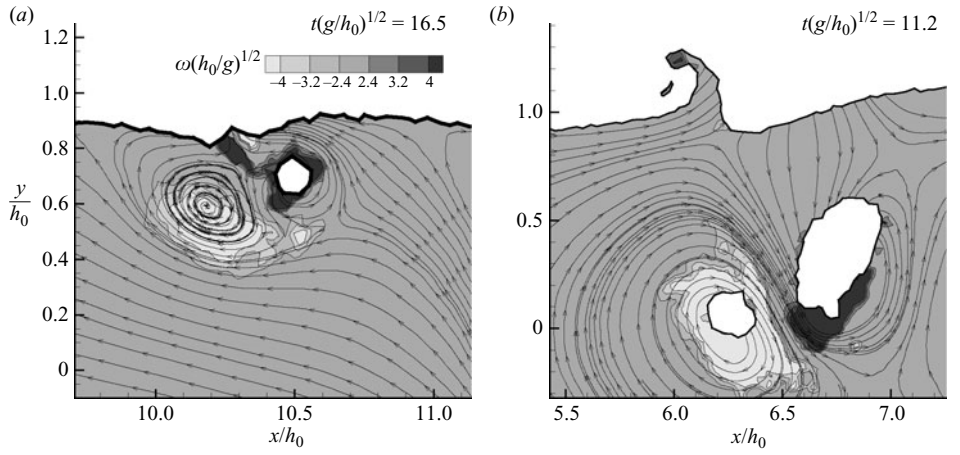

FIGURE 9. Enlarged view of the velocity field during SPH splash-up phenomena with features similar, respectively, to the (*a*) mode A and (*b*) mode B interactions described by Bonmarin (1989). Solid arrowed lines give an indication of the overall direction of motion and the contour levels represent the vorticity field. The phenomena shown correspond, respectively, to the splash-up events *II* and *I* described figure 8. Main parameters are defined in figure 2.

Examples of Mode A and Mode B interactions predicted by the SPH simulations are given in figure 9. They correspond, respectively, to the splashe-ups *II* and *I* described above in the text.

The genesis of any vortical region is related to a folding over of the surface which creates a doubly connected region. This aspect is crucial for the generation of vorticity and circulation (see i.e. Hornung, Willert & Turner 1995).

The rate of such formation is a measure of the flow-field unsteadiness. Here, the latter has been investigated numerically in terms of the frequency of creation of the forward splashes. As an example, the history of the vortical structures generated in the case $F_P = 0.8$ is reported in figure 10. The results indicate a non-zero and negative net vorticity in the fluid domain. This is consistent with the experimental observations by Miller (1976). The occurrence of non-zero net vorticity has an inviscid reason, that is cavity closure due to breaking, and is not in contrast with Kelvin's theorem for the circulation. A theoretical discussion about the vorticity generation in the context of wave breaking can be found, for instance, in Hornung *et al.* (1995).

In figure 10, the rotational areas are identified by the dashed lines and are numbered in order of appearance. During their evolution the vortical structures can tend either to pair or to break into multiple vortices. The latter circumstance occurs for the vortical structures 13 and 14 in figure 10(*f*).

In the Froude-number range considered, the first backward plunging jet is always rather strong. It impacts with the free surface and evolves according to the Bonmarin's mode B interaction. From the fragmented free surface, two vortical structures of opposite sign are created and shed. These will pair with each other and start to fall down. The next flow evolution is complex and characterized by the occurrence of additional mode B interactions and of less intense Mode A interactions. In the latter case, the vortices stay near the free surface longer. As the piston speed decreases, the intensity of the splashes reduces and the number of Mode A interactions increases with respect to that of Mode B interactions. This leads to a series of vortices interacting with each other and forming a sort of chain in proximity of the free surface.

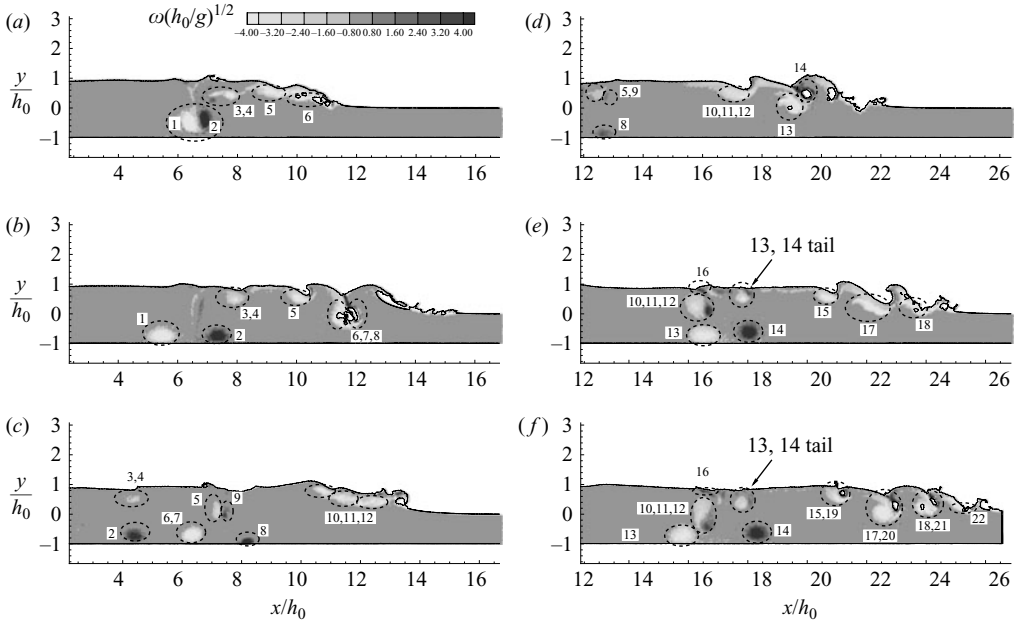

FIGURE 10. Breaking bore for piston-based Froude number $F_P = 0.8$: tracking of vortical structures generated during the splash-up cycles. They are highlighted through the vorticity contour levels and are numbered in order of appearance. Time increases from (*a*) to (*f*) with time instants $t(g/h_0)^{1/2} = 12.9$, 16.0, 20.7, 24.5, 29.9, 31.5. Main parameters are defined in figure 2.

In the following, the shedding phenomenon is investigated by considering different speeds of the bore front.

If $N_V(t;t_0)$ is the number of vortical structures generated in a time interval $(t - t_0)$, the averaged frequency of the shedding of vortices with the same sign results

$$f_s(t;t_0) = \frac{N_V(t;t_0)/2}{(t - t_0)}. \tag{3.8}$$

Here the initial time t_0 was chosen as the instant when the first plunging jet hits the free surface. If we takes the ratio $(h_1 - h_0)/u$ as the characteristic time scale for the bore evolution, a Strouhal number

$$St = f_s \frac{h_1 - h_0}{u} = f_s \sqrt{\frac{h_0}{g}} \Big/ \left(\frac{F_0}{h_1/h_0 - 1} \right), \tag{3.9}$$

related to the shedding phenomenon can be introduced. For a given time interval $[t_0, t]$, as F_0 decreases, the size of the generated vortical structures reduces and their number increases. This implies that f_s increases (see figure 11) and the trend is the same for $F_0/(h_1/h_0 - 1)$, so that St remains almost constant. This implies a correlation between the frequency of vortex creation and the strength of the bore. The value of St is about 0.22, which is almost the same as for the Strouhal number related to an analogous circular cylinder with a diameter $D = h_1 - h_0$, moving at a speed $U_\infty = u$ (cf. figure 12) and with Reynolds number in the subcritical regime (see e.g. Goldstein 1965).

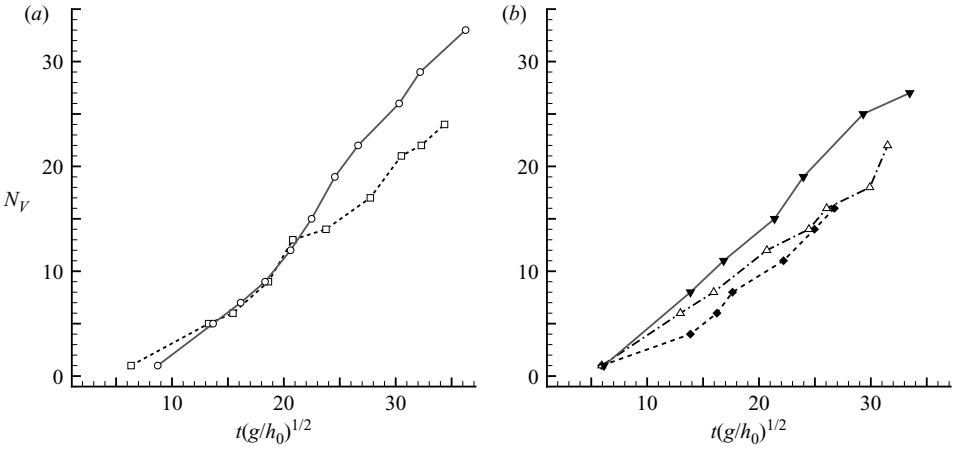

FIGURE 11. Time evolution of the number of vortices N_v generated during the bore propagation for different piston velocities. (*a*) ○, $F_P = 0.5$; □, $F_P = 0.6$. (*b*) ▼, $F_P = 0.7$; △, $F_P = 0.8$; ◆, $F_P = 0.9$. Main parameters are defined in figure 2.

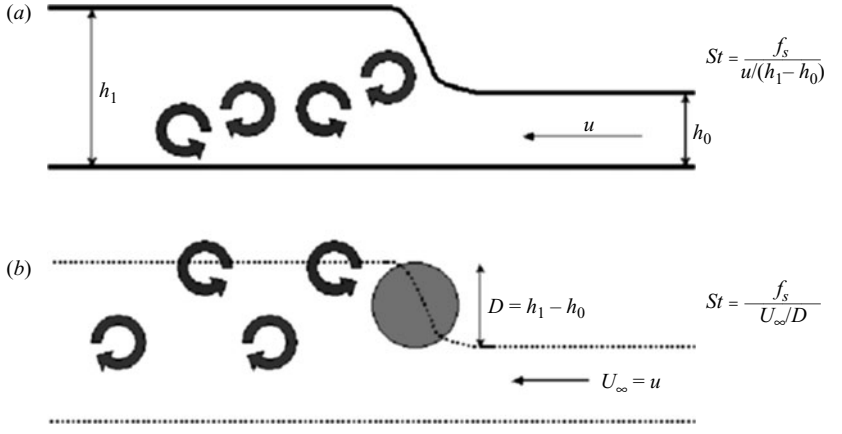

FIGURE 12. Definition of the Strouhal number. (*a*) Bore problem. u is the upstream current velocity seen by the front of the bore. h_0 and h_1 are the upstream and downstream water depths, respectively. (*b*) Analogous circular cylinder problem. U_∞ is the current velocity seen by the cylinder. D is the cylinder diameter. f_s is the frequency of the shedding of vortices with the same sign.

The results of this simplified analysis in terms of the main parameters involved are summarized in table 2.

3.4. *SPH simulation with local refinement*

A lower value of F_P leads to a smaller size of the initial plunging jet. Therefore a spatial discretization with a sufficiently small dx/h_0 is needed to capture the fluid structures originated during the splash-up phases. For instance, to ensure almost the same plunging jet resolution considered for the piston-based Froude number $F_P = 0.8$, in the case with $F_P = 0.5$ the number of particles has to pass from 80 000 to at least half million. This leads to very demanding CPU-time requirements. Therefore the cases with the smallest Froude numbers, $F_P = 0.5$ and 0.6, have been analysed by

F_P	F_0	$2\overline{f_s}\sqrt{h_0/g}$	$F_0/(h_1/h_0-1)$	$\overline{St}$
0.90	1.80	0.36	1.64	0.22
0.80	1.66	0.40	1.84	0.22
0.70	1.59	0.51	1.99	0.26
0.60	1.52	0.40	2.17	0.19
0.50	1.37	0.61	2.74	0.22

TABLE 2. Vortex creation during the splash-up cycles for different piston velocities. $\overline{f_s}$, $\overline{St}$ represent, respectively, the averaged values for the dimensionless frequency of shedding and for the Strouhal number defined in expressions (3.8) and (3.9). The average is taken during the last $10\sqrt{h_0/g}$ s of the bore propagation. Main parameters are defined in figure 12.

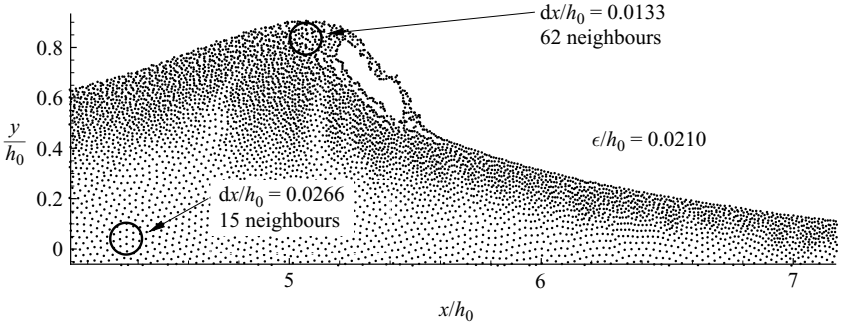

FIGURE 13. Non-uniform distribution of the SPH particles used to capture the first plunging jet induced by the piston-based Froude number $F_P = 0.5$. Close to the free surface, the particle distribution is four times denser than that used near the bottom. All the particles have the same $\epsilon/h_0 = 0.0210$, as a consequence the particles close to the free surface are characterized by a larger number of neighbours. The numerical parameters are defined in § 2.

introducing a local refinement only near the free surface to limit the required memory space and CPU time.

To avoid numerical complexities, ϵ has been kept constant (see Hernquist & Katz 1989; Nelson & Papaloizou 1994), therefore the smaller particles in proximity of the free surface have a large number of neighbours $\mathcal{N} > 50$, while the neighbours of the particles close to the bottom reduce to $\mathcal{N} = 15$. As an example, figure 13 shows the particle distribution used for $F_P = 0.5$. The SPH simulations performed with the described strategy are characterized by numerical noise due to coarser particle distributions in some fluid areas. In the present case, this occurs in the region beneath the bore front. Despite this, the numerical results are still reliable for a qualitative analysis of the breaking bore propagation.

4. Bores on beaches

The problem of the run-up of waves on sloping beaches is widely treated because of its practical importance, for example in the context of coastal erosion, flooding and tsunamis. Here we present some results for fully developed bores climbing up beaches with constant slope α. A sketch of the model problem with the relevant parameters is given in figure 14 where particles are marked according to their initial submergence. Following Miller (1968), the simulation starts with a piston which reaches its final velocity after a smooth acceleration. The piston maintains this speed

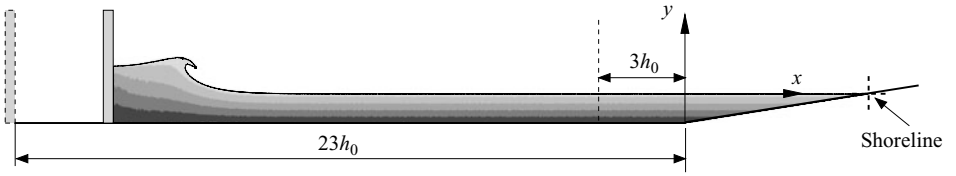

FIGURE 14. Numerical simulation of a breaking bore climbing an inclined beach. The mean water level is $h_0 = 0.1$ m. The piston starts to move at a distance $23h_0$ from the beach and stops at $3h_0$ from it. Main parameters are defined.

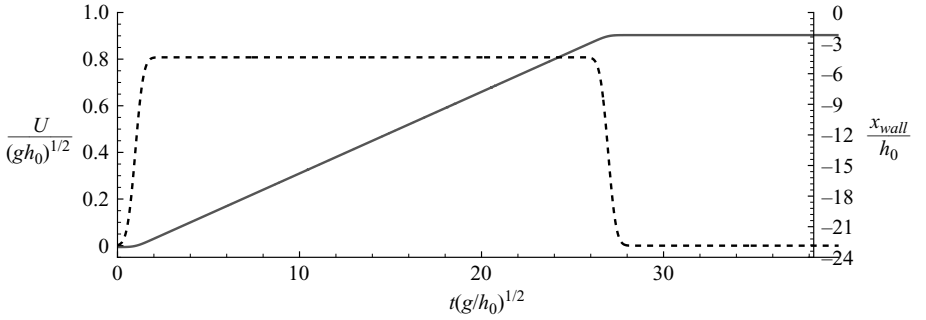

FIGURE 15. Breaking bore climbing an inclined beach: velocity (dashed line) law imposed to the piston and corresponding position (solid line) as a function of time. The piston starts to move with a smooth acceleration and reaches a final velocity which is maintained constant for about $25\sqrt{h_0/g}$ s. During this time interval, a fully developed breaking bore is formed. At a distance $3h_0$, far from the beach, the piston stops its forward motion with a smooth deceleration, while the bore propagates shoreward. Main parameters are defined in figure 14.

for a certain time interval and then stops its forward motion (see figure 15). This leaves a fully developed breaking bore propagating shoreward, through water with decreasing depth, collapsing down after reaching the shoreline, and eventually entering a running-up mode where splashing at the front is not detected anymore. As observed by Yeh, Ghazali & Marton (1989), the evolution of an undular bore would be rather different, with the bore front steepening, overturning and plunging onto the dry beach. This case is not studied here.

The description of the region where the water front meets the beach is numerically challenging because of the low density of involved particles. This leads to an inevitable loss of accuracy. However, such a local deficiency has a limited role for the main flow features which are dominated by the incoming finite-water wave.

The evolution for a piston-based Froude number $F_P = 0.8$ and a beach with constant slope $\alpha = 3^\circ$ is shown in figure 16. In this case, h_0 is the uniform depth before the sudden change in the slope. In figure 16(*a*), the bore front propagates along an essentially unperturbed layer of water with decreasing depth. The typical character of the bore, i.e. a steep jump reconciling water of different depths, is preserved in figures 16(*b*) and 16(*c*), where the bore approaches the shoreline.

Ho & Meyer (1962) analysed theoretically the evolution of a fully developed bore approaching the shoreline. In their shallow-water theory, the bore is modelled as a sharp discontinuity in height and velocity, and the shoreline is a singular point of the solution. Within this framework, the bore height decreases as the square root of the distance from the shoreline, ultimately disappearing at the singular point. Such

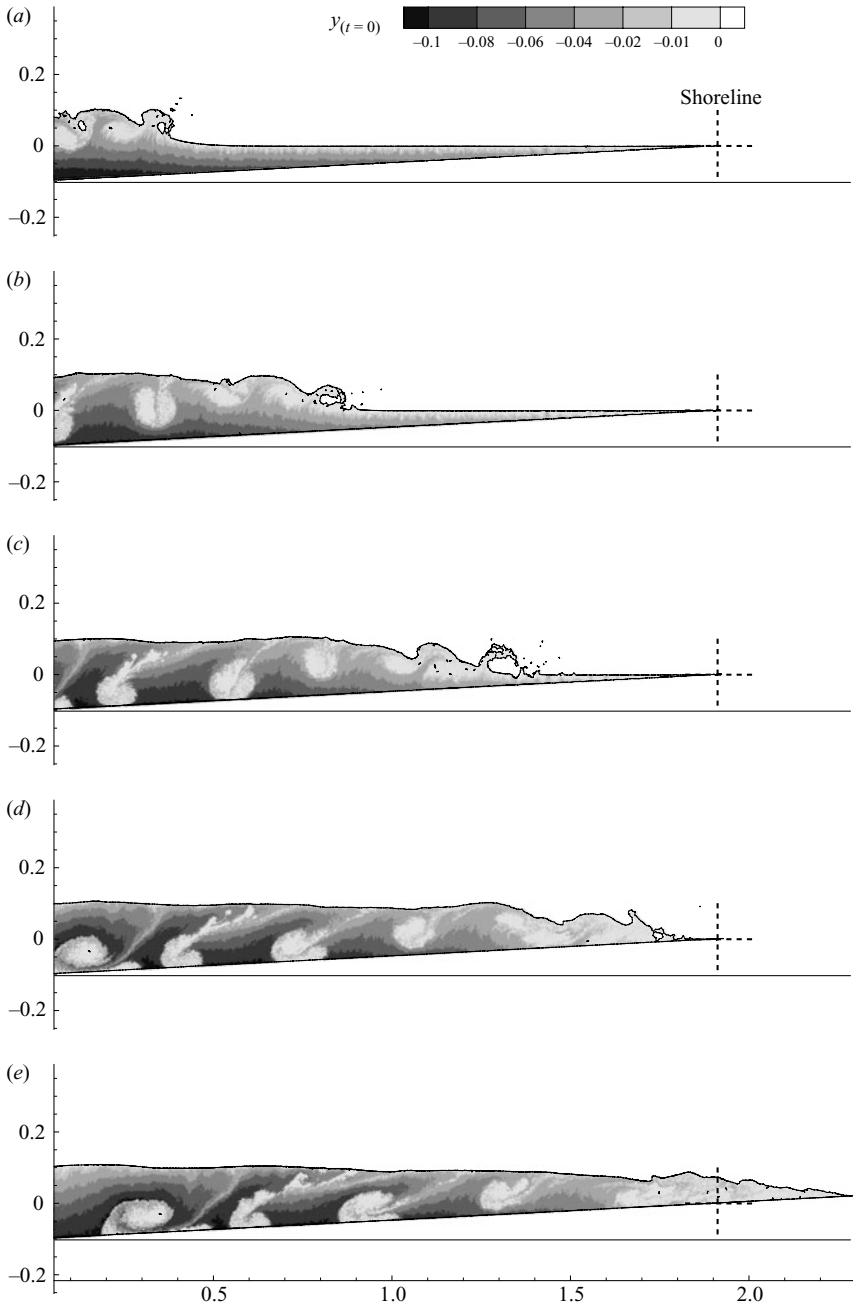

FIGURE 16. Breaking bore climbing an inclined beach: run-up of the bore generated by a piston initially moving with a Froude number $F_P = 0.8$, along a beach with constant slope $\alpha = 3^\circ$. The crosses mark the shoreline and the contour levels are representative of the vertical heights $y_{(t=0)}$ at initial time $t = 0$ s of the particles simulated by the SPH. The evolution shows an important fluid mixing with initially free-surface particles migrating toward the beach. The transport of surface water shorewards, and advected to the bed by vortex pairs, is nicely shown by these results. (*a*) to (*e*) correspond to time instants $t\sqrt{g/h_0} = 17$, 19.9, 22.4, 25, 27.7, respectively. In the numerical simulation $h_0 = 0.1$ was used. Main parameters are defined in figure 14.

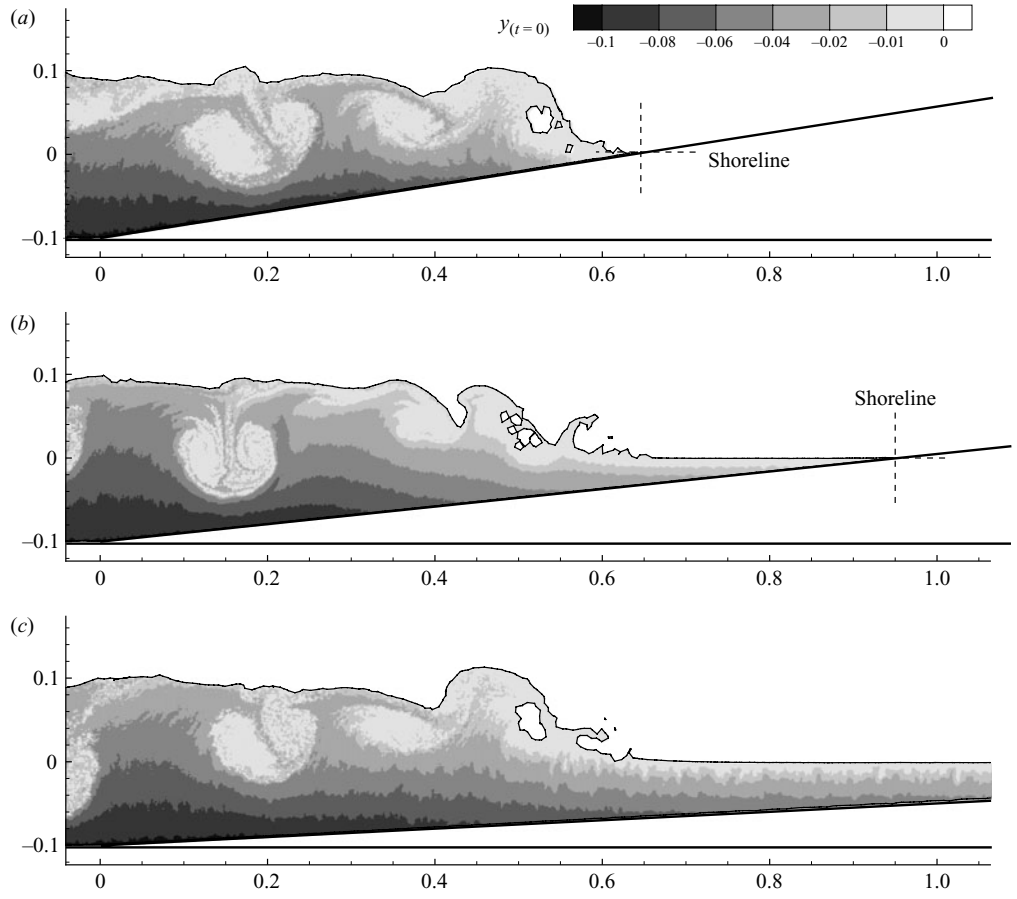

FIGURE 17. Breaking bore climbing an inclined beach: snapshot of the bore front at $t\sqrt{g/h_0} = 18.66$ for piston-based Froude number $F_P = 0.8$ and decreasing slope, α, of the beach. (*a*) $\alpha = 9°$, (*b*) $\alpha = 6°$, (*c*) $\alpha = 3°$. The three simulations have been stopped at the same time: the comparison shows the waves at similar x-coordinate positions. For $\alpha = 9°$, the bore reached the shoreline. In the numerical simulation, $h_0 = 0.1$ was used. Contour levels are representative of the vertical heights $y_{(t=0)}$ at initial time $t = 0$ s of the particles simulated by the SPH. Main parameters are defined in figure 14.

'bore collapse' was observed numerically by Keller, Levine & Witham (1960) and agrees qualitatively with experiments (Miller 1968; Yeh *et al.* 1989) and with our numerical observations.

In the later evolution, breaking seems to cease (figure 16*e*). A more detailed analysis reveals a gradual reduction of the steepness of the bore front, which at the shoreline reduces to a fluid wedge propagating shoreward. Further, from the shoreline on, the flow resembles that generated after a dam break. In more detail, shallow-water theory (Stoker 1957), experiments, and our numerical simulations (not reported here) show the water front propagating smoothly along the beach without breaking.

Figure 17 presents the water configurations and the flow fields for three slopes of the beach, at the same time instant from the starting of the piston motion. As α increases, the bore becomes closer to the shoreline. For the steepest beach, it has already reached the shoreline and is almost ready to collapse, as described above. In all cases, the front of the bore is located practically at the same abscissa, showing the

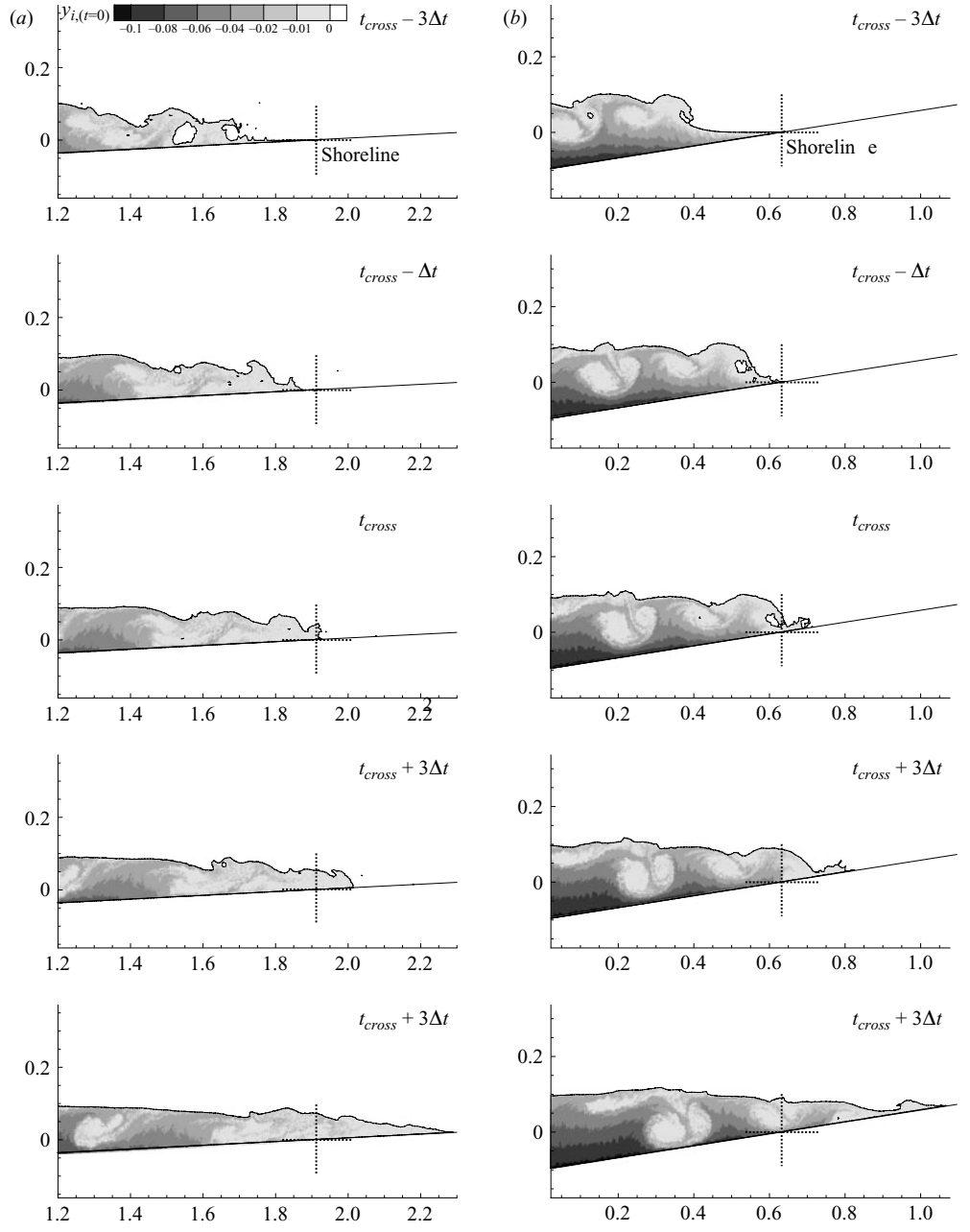

FIGURE 18. Breaking bore climbing an inclined beach: evolution of the bore front while going through the shoreline for a piston-based Froude number $F_P = 0.8$. (*a*) $\alpha = 3^\circ$, $t_{cross}\sqrt{g/h_0} = 26.13$, $\Delta t\sqrt{g/h_0} = 0.53$. (*b*) $\alpha = 9^\circ$, $t_{cross}\sqrt{g/h_0} = 18.66$, $\Delta t\sqrt{g/h_0} = 0.53$. Contour levels are representative of the vertical heights $y_{(t=0)}$ at initial time $t = 0$ s. of the particles simulated by the SPH. Main parameters are defined in figure 14.

limited role of the beach slope in altering the bore celerity. It is remarkable that the structures of the bore front remain similar despite the different beach angles.

Figure 18 shows the details of the bore-front evolution while crossing the shoreline, for $\alpha = 3^\circ$ and 9°. In both cases, the evolution of the field shade levels highlights the

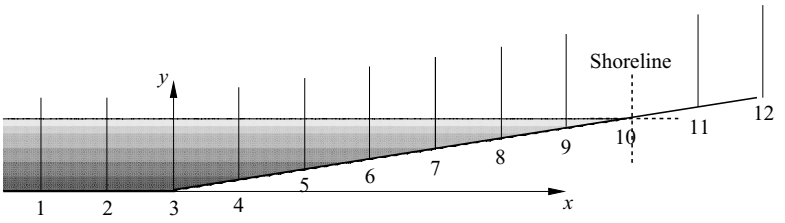

FIGURE 19. Breaking bore climbing an inclined beach: positions of the vertical fixed sections where velocity vector profiles are calculated during the SPH simulation (solid lines).

migration rightwards of the initially near free-surface particles. It shows also their migration toward the inclined sea floor as an interesting feature for the flow up a beach.

For the largest slope, the bore front reaches the shoreline in a rather violent way: the amount of water involved is greater and the vortical structures behind the bore front are bigger and more intense than for smaller α. Once the bore has collapsed against the shoreline, the vortices already shed are convected forward by the main flow and go beyond the shoreline. They could be responsible for beach erosion which is quite relevant in practice. For $\alpha = 3^\circ$, the beach is almost three times longer than for $\alpha = 9^\circ$. As a result, the mechanical energy of the bore is dissipated in a larger sea bottom length and the flux of the fluid momentum at the shoreline is smaller than for $\alpha = 9^\circ$. In particular, the layer of fluid at the shoreline is thinner and the convected vortical structures are more stretched and smaller.

4.1. *Bore approaching the beach: velocity profiles*

The velocity field associated with the evolution of a bore approaching a straight inclined beach has been studied by estimating the velocity vector profiles at the twelve fixed vertical sections shown in figure 19. The two most upstream sections are located before the beach, where the water depth is constant. The others are in the beach region with the last two beyond the shoreline and therefore wetted only once the front of the bore has passed their location.

In the following, the case with a beach slope $\alpha = 3^\circ$ is considered. The velocity profiles, calculated by using the interpolation integral introduced in § 2, are given in figure 20 at different time instants. At the first time instant shown, the front of the bore is between the two most advanced sections. Owing to the passage of the bore front propagating with a velocity $u = 1.66\sqrt{gh_0}$, near the free surface the velocity profile recorded along section 1 is characterized by high horizontal values, while close to the bottom these are similar to the piston velocity $U = 0.8\sqrt{gh_0}$. In figure 20(*b*), the bore front has reached section 2. The velocity profile here is similar to that observed at the previous time instant along section 1. At this stage, a dipole structure is visible near the sea bottom. As time goes on, the two vortical structures move in opposite direction along the seabed. When the clockwise vortex reaches section 1 the resulting velocity profile is characterized by large gradients near the bottom (see figure 20*d*). In figure 20(*e*) the core of the counterclockwise vortex is almost at section 2. Also, this vortex induces a large velocity gradient, but with opposite sign with respect to the clockwise structure. In more detail, the counterclockwise vortical structures are responsible for high tangential velocities on the seabed.

In the present simulations, the sea-floor boundary layer is not modelled; however, the results suggest the occurrence of high shear stresses at the bottom. At the sections not influenced by the front of the bore and by the vortical structures, the

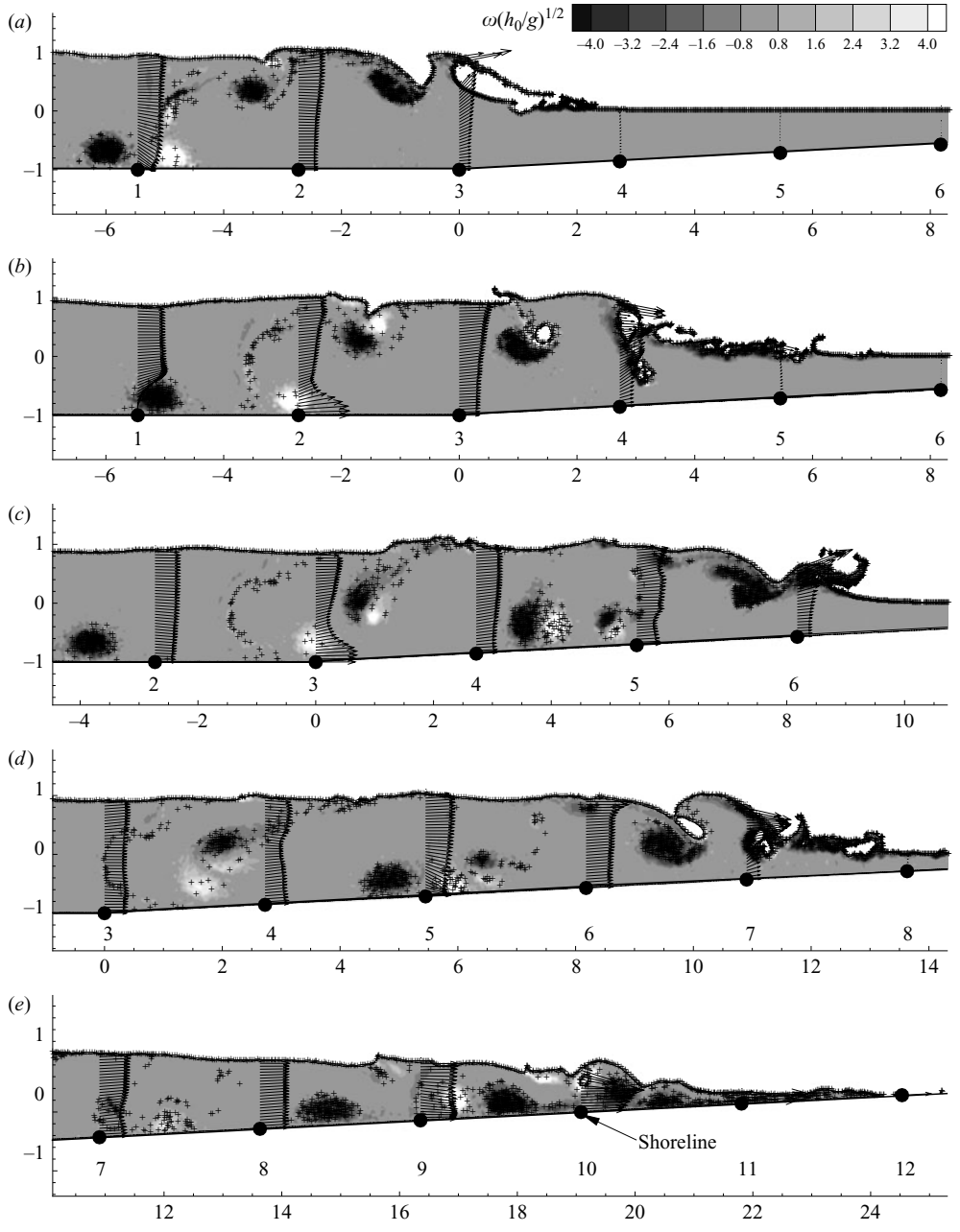

FIGURE 20. Breaking bore climbing an inclined beach: vorticity contour levels in the flow field and vector velocity profiles at the fixed vertical sections defined in figure 19. $U = 0.8\sqrt{gh_0}$ and $\alpha = 3°$. The small dots are the particles which belong to the free surface at initial time $t = 0$. These particles have been trapped into the fluid during the breaking processes. The time increases from (*a*) to (*e*), $t(g/h_0)^{1/2} = 14.9$, 16.8, 19.8, 21.8, 27.7.

velocity profiles appear more regular, with almost zero vertical component and with a horizontal value close to the piston velocity (see e.g. along section 2 in snapshot *a* of the figure). In the snapshots (*d*, *e*) of figure 20, the bore front propagates along the

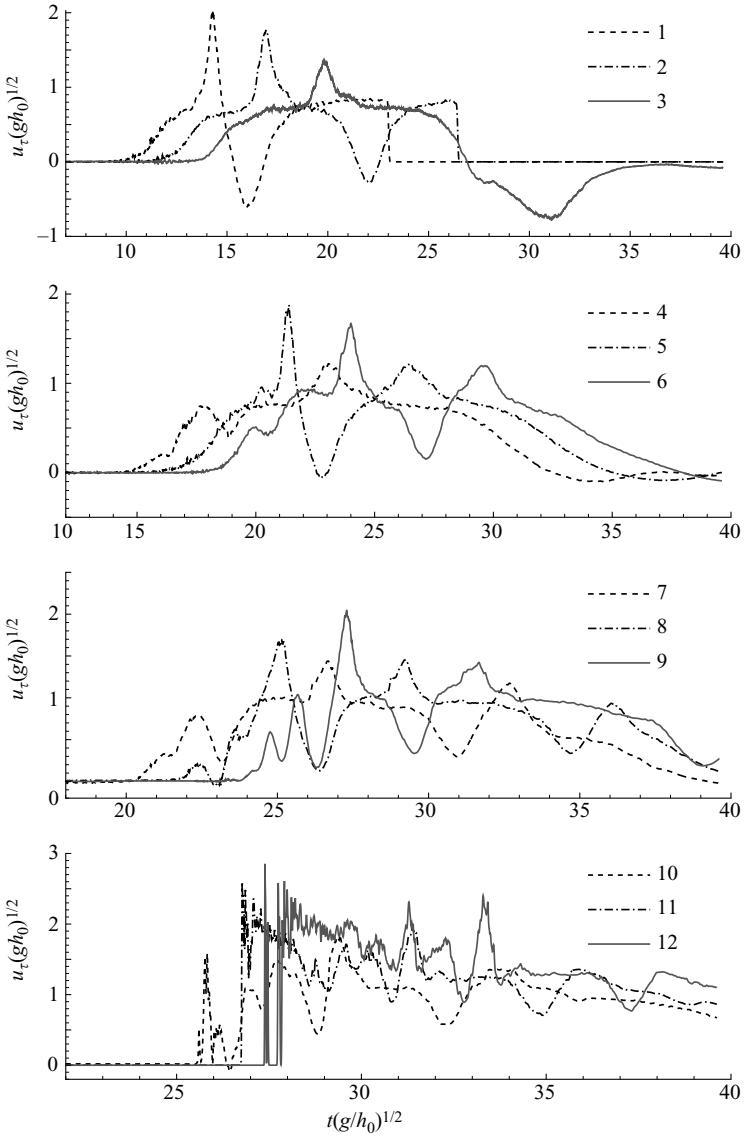

FIGURE 21. Breaking bore climbing an inclined beach: time histories of the sea-floor tangential velocity, u_τ, at the fixed sections defined in figure 19 (the numbers are consistent with those of the twelve probes). $U = 0.8\sqrt{gh_0}$ and $\alpha = 3^\circ$.

inclined beach and the vortical structures interact with the local sea floor soon after they have been created. As a consequence, close to the bottom the velocity profiles are characterized by large horizontal and vertical velocity gradients. When the bore front reaches the shoreline a high-speed tongue of fluid is created and starts to rise along the initially dry beach. At this stage no additional vortical structures are generated.

Figure 21 shows the time histories of the sea-floor tangential velocities u_τ at the different vertical sections. All nine probes upstream the shoreline show large fluctuations due to the interaction with the vortical structures shed from the breaking-bore front. For almost all locations, the maximum velocity recorded exceeds the speed of the

bore front. At sections 1 and 3, the tangential velocities even become negative owing to the interaction with a strong vortical dipole structure. The latter is released by the breaking-bore front during its propagation in the constant-water-depth region. This is the first double-vortical structure generated by the breaking bore; it is characterized by a stronger intensity with respect to the following ones. The time histories of the tangential velocity for the first two probes fall to zero once the piston has reached their positions during its slowdown stage.

The highest values of u_τ have been recorded at the last three probes which correspond to the shoreline area. Such values are related to the 'bore collapse', when the flow locally resembles that after a dam break.

5. Discussion and summary

A numerical code to simulate flows with free-surface and breaking fragmentation has been developed and applied to study the genesis and evolution of breaking bores running on uniform and sloped bottoms. The solver is based on a gridless particle method (SPH) for the Euler equations and features a Lagrangian character which allows us to track in detail the complex dynamics of the breaking bore front.

Splash-up cycles and their link with the genesis of vortical structures downstream of the bore are discussed in detail. The presence of vortical structures of both signs is detected and connected with the splash-up mechanics, characterized by the formation of mushroom-like upwelling structures with one branch folding backward and creating circulation of opposite sign with respect to the forward plunging breaker. The SPH predicted evolution of the bore breaking appeared very similar to the experimental observations by Bonmarin (1989) for deep-water breaking waves.

A remarkable feature of the observed motion is the complex behaviour of the free surface, creating holes, circulation and vorticity shed into the wakes, forming coherent structures. These result in large-scale convection and mixing of fluids, impacts on the bottom and scouring velocities at the sea bed.

According to the analysis, vortices with opposite sign can pair to form dipole structures. These affect the water evolution and can interact in a complex way with the free surface and with the sea floor. In the latter case, large stresses can be induced at the bottom that are responsible for erosion.

The investigation is extended to the case of breaking bores climbing sloped beaches and the mechanics of propagation through the shoreline is discussed. From the results, the essential character of the bore which propagates through splash-up cycles is preserved up to the shoreline. The splashing ceases when the bore reaches the dry beach; after that the front seems to propagate smoothly and without breaking and resembles the motion after a dam break.

The extension of the Lucy–Monaghan SPH method described here, and its intensive application to breaking bores as well as to strong breaking flows at the bow and stern of ships, originated in an Office of Naval Research program aimed at the prediction of air entrainment from breaking waves produced at the bow and stern of fine naval vessels. The ONR Program Manager was then Dr Edward Rood, jr. The original work was carried out in The Ocean Engineering Laboratory of the University of California at Santa Barbara and began in 1998. The Principal Investigator was Professor Marshall P. Tulin, the Director of the OEL. We are grateful to Dr Rood and the ONR for their support.

In the beginning years, 1998–2000, the work involved the collaboration of INSEAN personnel from Rome who worked at the OEL in the ONR Program, and particularly of Dr Maurizio Landrini who is the principal architect of the detailed computational techniques described here. This collaboration, was made possible by the management of INSEAN, Admiral Ulderico Grazioli, and Dr Ulderico Paolo Bulgarelli. We are very grateful to them for this, and for allowing and encouraging further work to be carried out in Rome by INSEAN personnel after 2000, and in the preparation of this paper after 2003, when Maurizio Landrini died in a motorcycle accident in central Rome, a tragic loss to the field of Naval Hydrodynamics.

REFERENCES

Abadie, S., Caltagirone, J. & Watremez, P. 1998 Splash-up generation in a plunging breaker. *C. R. Acad. Sci. Paris* IIB *Mech. Phys. Astron.* **326**(9), 553–559.

Allen, M. P. & Tildesley, D. J. 1987 *Computer Simulation of Liquids*. Oxford.

Battjes, J. A. 1988 Surf-zone dynamics. *Annu. Rev. Fluid Mech.* **20**, 257–291.

Belytschko, T., Lu, Y. Y. & Gu, L. 1994 Element free Galerkin. *Intl J. Numer. Meth. Engng* **37**, 229–256.

Belytschko, T., Krongauz, Y., Organ D., Fleming M. & Krysl P. 1996 Meshless methods: an overview and recent developments. *Comput. Meth. Appl. Mech. Engng* **139**, 3–47.

Belytschko, T., Krongauz, Y., Dolbow, J. & Gerlach, C. 1998 On the completeness of meshfree particle methods. *Intl J. Numer. Meth. Engng* **43**, 785–819.

Benz, W. 1990 Smooth particle hydrodynamics: a review. In *The Numerical Modelling of Nonlinear Stellar Pulsation* (ed. J. R. Buchler), pp. 269–288 Kluwer.

Bicknell, G.V. 1991 The equations of motion of particles in smoothed particle hydrodynamics. *SIAM J. Sci. Statist. Comput.* **12**(5), 1198–1206.

Bonet, J. & Lok, T.-S. L. 1999 Variational and momentum preservation aspects of SPH formulations. *Comput. Meth. Appl. Mech. Engng* **180**, 97–115.

Bonmarin, P. 1989 Geometric properties of deep-water breaking waves. *J. Fluid Mech.* **209**, 405–433.

Bradford, S. F. 2000 Numerical simulation of surf zone dynamics. *J. Waterway Port Coastal Ocean Engng* **126**(1), 1–13.

Chen, G., Kharif, C., Zaleski, S. & Li, J. 1999 Two-dimensional Navier–Stokes simulations of breaking waves. *Phys. Fluids* **11**(1), 121–133.

Christensen, E. D. & Deigaard, R. 2001 Large eddy simulation of breaking waves. *Coast. Engng* **42**(1), 53–86.

Cointe, R. & Tulin, M. P. 1994 A theory of steady breakers. *J. Fluid Mech.* **276**, 1–20.

Colagrossi, A. 2005 A meshless Lagrangian method for free–surface and interface flows with fragmentation. PhD thesis, Department of Mechanical Engineering, University of Rome, 'La Sapienza' (http://padis.uniroma1.it).

Colagrossi, A. & Landrini, M. 2003 Numerical simulation of interfacial flows by smoothed particle hydrodynamics. *J. Comput. Phys.* **191**, 448–475.

Colagrossi, A., Landrini, M. & Tulin, M. P. 2000 Near shore bore propagation and splashing processes: gridless simulations. *Proc. 6th Intl Workshop on Wave Hindcasting and Forecasting*. Metereological Service of Canada, Monterey, CA.

Colicchio, G., Colagrossi, A., Greco, M. & Landrini, M. 2002 Free-surface flow after a dam Break: a comparative study. *Ship Technol. Res.* **49**(3), 95–104.

Di Lisio, R., Grenier, E. & Pulvirenti, M. 1998 The convergence of the SPH Method. *Comput. Maths Applics* **35**(1), 95–102.

Dold, J. W. & Peregrine, D. H. 1986 An efficient boundary integral method for steep unsteady water waves. *Numerical Methods for Fluid Dynamics II* (ed. K. W. Morton & M. J. Baines), pp. 671–679. Oxford University Press.

Fries, T. P. & Matthies, H. G. 2004 Classification and overview of meshfree methods. *Informatikbericht 2003-03, Institute of Scientific Computing, Technical University Braunschweig, Brunswick, Germany, 2003.*

Gingold, R. A. & Monaghan, J. J. 1977 Smoothed particle hydrodynamics: theory and application to non spherical stars. *Mon. Not. R. Astr. Soc.* **181**, 375–389.

Goldstein, S. 1965 *Modern Developments in Fluid Dynamics*. Dover.

Greenhow, M. & Lin, W. M. 1985 Numerical simulation of nonlinear free-surface flows generated by wedge entry and wavemaker motions. *Proc. 4th Intl Conf. on Numerical Ship Hydrodynamics, Washington-DC, USA*.

Grilli, S., Svendsen, A. & Subramanya, R. 1997 Breaking criterion and characteristics for solitary waves on slopes. *J. Waterway Port Coastal Ocean Engng* **123**, 102–112.

Hernquist, L. & Katz, N. 1989 TREESPH: a unification of SPH with the hierarchical tree method. *Astrophys. J. Suppl. Ser.* **70**, 419–446.

Ho, D. V. & Meyer, R. E. 1962 Climb of a bore on a beach. Part 1. Uniform beach slope. *J. Fluid Mech.* **14**, 305–318.

Hornung, H. G., Willert, C. & Turner S. 1995 The flow field downstream of a hydraulic jump. *J. Fluid Mech.* **287**, 299–316.

Jansen, P. 1986 Laboratory observations of the kinematics in the aerated region of breaking waves. *Coastal Engng* **9**, 453–477.

Keller, H. B., Levine, D. A. & Witham, G. B. 1960 Motion of a bore over a sloping beach. *J. Fluid Mech.* **7**, 302–315.

Lamarre, E & Melville W. K. 1991 Air entrainment and dissipation in breaking waves. *Lett. Nature* **341**, 469–472.

Landrini, M. & Tyvand, P. A. 2001 Generation of water waves and bores by impulsive bottom flux. *J. Engng Maths* **39**, 131–170.

Landrini, M., Colagrossi, A. & Tulin, M. P. 2001 Breaking bow and stern waves: numerical simulations. *Proc. 16th Intl Workshop on Water Waves and Floating Bodies, Hiroshima, Japan.*

Landrini, M., Colagrossi, A. & Faltinsen, O. M. 2003 Sloshing in 2-D flows by the SPH method. *Proc. 8th Intl Conf. on Numerical Ship Hydrodynamics, Busan, South Korea.*

Lemos, C. M. 1996 Higher-order schemes for free-surface flows with arbitrary configurations. *Intl J. Numer. Meth. Fluids* **23**, 545–566.

Le Touzé, D. & Colagrossi, A. 2005 Free-surface prototype problems suitable to investigate particle methods. *Proc. 20th Intl Workshop on Water Waves and Floating Bodies, Longyearbyen, Norway.*

Lin, C. & Hwung, H. H. 1992 External and internal flow fields of plunging breakers. *Exps. Fluids* **12**, 229–237.

Lin, P. & Liu, P. L.-F. 1998 A numerical study of breaking waves in the surf zone. *J. Fluid Mech.* **359**, 239–264.

Lin, P. & Liu, P. L.-F. 1999 Free-surface tracking methods and their applications to wave hydrodynamics. *Adv Coastal Ocean Engng* **5**, 213–240.

Lucy, L. B. 1977 A numerical approach to the testing of fission hypothesis. *Astron. J.* **82**(12), 1013–1024.

Mas-Gallic, S. & Raviart, P. A. 1987 A particle method for first-order symmetric systems. *Numerische Mathematik* **51**(3), 323–352, July.

Miller, R. L. 1968 Experimental determination of run-up of undular and fully developed bores. *J. Geophys. Res.* **73**(14), 4497–4510.

Miller, R. L. 1976 Role of vortices in surf-zone prediction: sedimentation and wave forces. *Soc. Economic Paleontologists and Mineralogists Special Publication* (ed. R. A Davis & R. L. Ethington) **24**, 92–114.

Molteni, D., Colagrossi, A. & Colicchio G. 2007 On the use of an alternative water state equation in SPH. *Proc. SPHERIC, 2nd Intl Workshop, Universidad Politécnica de Madrid, Spain, May*, pp. 23–26.

Monaghan, J. J. 1985 Particle methods for hydrodynamics. *Comput. Phys. Rep.* **3**(2), 71–124.

Monaghan, J. J. 1992 Smoothed particle hydrodynamics. *Annu. Rev. Astron. Astrophys.* **30**, 543–574.

Monaghan, J. J. 1994 Simulating free surface flows with SPH. *J. Comput. Phys.* **110**, 399–406.

Monaghan, J. J. 2005 Smoothed particle hydrodynamics. *Rep. Prog. Phys.* **68**, 1703–1759.

Monaghan, J. J. & Gingold, R. A. 1983 Shock simulation by the particle method SPH. *J. Comput. Phys.* **52**, 374–389.

Monaghan, J. J. & Kos, A. 1999 Solitary waves on a Cretan beach. *J. Waterway Port Coastal Ocean Engng* **125**(3), 145–154.

Monaghan, J. J. & Kos, A. 2000 Scott Russell's wave generator. *Phys. Fluids* **12**(3), 622–630.

Monaghan, J. J., Kos, A. & Issa, N. 2003 Fluid motion generated by impact. *J. Waterway Port Coastal Ocean Engng* **129**(6), 250–259.

Morris, J. P. 1996 A study of the stability properties of smooth particle hydrodynamics. *Publ. Astron. Soc. Australia* **13**(1), 97–102.

Morris, J. P., Fox, P. & Zhu Y. 1997 Modeling low Reynolds number incompressible flows using SPH. *J. Comput. Phys.* **136**, 214–226.

Moussa, B. B. & Vila, J. P. 2000 Convergence of SPH method for scalar nonlinear conservation laws. *SIAM J. Numer. Anal.* **37**, 863–887.

Nelson, R. P. & Papaloizou, J. 1994 Variable smoothing lengths and energy conservation in smoothed particle hydrodynamics. *Mon. Not. R. Astron. Soc.* **270**, 1–20.

Peregrine, D. H. 1983 Breaking waves on beaches. *Annu. Rev. Fluid Mech.* **15**, 149–178.

Raviart, P. A. 1985 An analysis of particle methods. *Numerical Methods in Fluid Dynamics* (ed. F. Brezzi) Lecture Notes in Mathematics, vol. 1127, pp. 243–324. Springer.

Stoker, J. J. 1957 *Water Waves: the Mathematical Theory with Applications.* Interscience.

Svendsen, I. A., Madsen, P. A. & Hansen, J. B. 1978 Wave characteristics in the surf zone. *Proc. 16th Coastal Engineering Conf. ASCE, Hamburg, Germany*, pp. 520–539.

Takeda, H., Miyama, S. M. & Sekiya, M. 1994 Numerical simulation of viscous flow by smoothed particle hydrodynamics. *Prog. Theoret. Phys.* **92**(5), 939–960.

Teles da Silva, A. F. & Peregrine, D. H. 1990 Unsteady free surface waves by domain decomposition approach. *Proc. 16th Intl Workshop of Water Waves and Floating Bodies, Hiroshima, Japan.*

Trivellato, F., Bertolazzi, E. & Colagrossi, A. 2004 Two flow solvers for liquid–liquid impacts. *Vorticity and Turbulence Effects in Fluid–Solid Interactions, Advanced Fluid Mechanics.* WIT Press.

Tulin, M. P. & Landrini, M. 2000 Breaking waves in the ocean and around ships. *Proc. 23rd Symp. on Naval Hydrodyn.* vol. 4, pp. 1–32. National Academy Press, Val de Reuil, France.

Wang, P., Yao, Y. & Tulin, M. P. 1995 An efficient numerical tank for nonlinear water waves based on the multi-subdomain approach with BEM. *Intl J. Numer. Meth. Fluids* **20**, 1315–1336.

Welton, W. C. & Pope, S. B. 1997 PDF model calculations of compressible turbulent flows using smoothed particle hydrodynamics. *J. Comput. Phys.* **134**, 150–168.

Yeh, H., Ghazali, A. & Marton, I. 1989 Experimental study of bore run-up. *J. Fluid Mech.* **207**, 563–578.